Cryo-EM led analysis of open and closed conformations of Chagas vaccine candidate TcPOP and its antibody response characterisation

Sagar Batra[1,2†], Francisco Olmo[3†], Timothy J Ragan [4], Merve Kaplan[5,6], Valeria Calvaresi [5,6], Asger Meldgaard Frank [7], Claudia Lancey [4], Mahya Assadipapari [8,] Cuifeng Ying [8], Weston B. Struwe [5,6], Emma Hesketh [4], John M. Kelly[9], Lea Barfod [6,] and Ivan Campeotto[1]*

1. School of Biosciences, Division of Microbiology, Brewing and Biotechnology, University of Nottingham, Sutton Bonington Campus, Loughborough, LE12 5RD, UK
2. Interdisciplinary Biomedical research Center, School of Science and Technology, Nottingham Trent University, NG11 8NS, UK
3. Department of Parasitology, Faculty of Sciences, University of Granada, Granada, Spain.
4. Leicester Institute of Structural and Chemical Biology, University of Leicester, Lancaster Road, Leicester, LE1 7RH, UK
5. Physical and Theoretical Chemistry Laboratory, Department of Chemistry, University of Oxford, South Parks Road, OX1 3TA, UK.
6. The Kavli Institute for Nanoscience Discovery, Dorothy Crowfoot Hodgkin Building,University of Oxford, OX1 3QU, UK.
7. Department of Immunology and Microbiology, Centre for Medical Parasitology, Faculty of Health and Medical Sciences, University of Copenhagen, Copenhagen, DK
8. Advanced Optics & Photonics Laboratory, Department of Engineering, School of Science & Technology, Nottingham Trent University, Nottingham NG11 8NS, UK
9. Department of Infection Biology, Faculty of Infectious and Tropical Diseases, London School of Hygiene and Tropical Medicine, Keppel Street, London, WC1E 7HT

*correspondence: ivan.campeotto@nottingham.ac.uk
† equal author contribution

Keywords: Chagas disease, cryo-EM, enzymology, SAX, MD, plasmonic optical tweezers, HDX-MS, neutralizing antibodies

Abstract

Chagas disease, caused by the protozoan parasite *Trypanosoma cruzi*, remains a significant global public health concern. Despite its profound health impact in both endemic and non-endemic areas, no vaccine is available, and the existing therapies are outdated, producing severe side effects. The 80kDa prolyl oligopeptidase of *Trypanosoma cruzi* (TcPOP) has been recently identified as a leading candidate for Chagas vaccine development. We report the first three-dimensional structure of TcPOP in open and closed conformation, at a global resolution of 3.8 and 3.6 Å respectively, determined

using single-particle cryo-electron microscopy. Multiple conformations were observed and further characterized using plasmonic optical tweezers and hydrogen-deuterium exchange mass spectrometry. To assess the immunogenic potential of TcPOP, we immunized mice and evaluated both polyclonal and monoclonal responses against the TcPOP antigen and its homologues. The results revealed invasion blocking properties of anti-TcPOP polyclonal response via parasite lysis and its cross-reactivity versus closely-related POPs but not with human homologues. We were also able to produce and characterise three monoclonal antibodies, one of which showed neutralising properties and inhibition of parasite invasion via non-lytic mechanism. Collectively, our findings provide critical structural and functional insights necessary to understand the immunogenicity of TcPOP for future Chagas vaccine development and diagnostic applications.

INTRODUCTION

Chagas disease is a chronic life-threatening parasitic disease caused by *Trypanosoma cruzi* and represents a significant health burden in 21 countries of Latin America[1]. Chagas continues to expand beyond endemic zones because of human migration and global warming[2], with 6 million infected people worldwide, leading to approximately 12,000 deaths per year (PANHO [3]). The major transmission route is via the bite of insects belonging to the Triatomine species bug in endemic regions, although other routes include congenital transmission, organ transplants, blood transfusion or oral transmission [4].

Chagas disease becomes symptomatic during the chronic stage when muscle cells in the heart and gut are compromised by both infection and immune responses against the parasite; this results in cumulative damage that leads to severe cardiac complications and heart failure in approximately 30% of patients, with an estimated global economic hardship of $7.19 billion US per year[5]. Chagas is therefore, one of the major global neglected tropical diseases (NTDs). There is no vaccine, and current therapy relies on the usage of the drugs nifurtimox and benznidazole[6], which can cause severe side effects including sterility, blindness, and deleterious effects in adrenal, colon, oesophageal and mammary tissue [7]. Additionally, therapies are more effective during the acute phase of the disease, and less so during chronic phase. Infection with *T. cruzi* is generally considered to be life-long, therefore representing a “time bomb” on the health systems around the world.

To complicate the epidemiological scenario, due to the evolutionary plasticity of *T.cruzi*, there are six discrete typing units (DTUs)[8] found to infect humans. An additional DTU has been identified in bats (Tcbat), although transmission to humans has not been yet reported[9]. DTUs differ in geographical and

ethnic distribution, clinical manifestations, and reservoir hosts, which include more than 150 species of mammals [10].

Diagnostic tools are often strain specific and unable to detect congenital transmission in newborn babies for the first 6 months, due to passive immunity from the mother, which can cause life-threatening complications later in life (PANHO[11]). Amidst these challenges, a member of the endopeptidase enzyme family, *T. cruzi* 80kDa prolyl-oligopeptidase (TcPOP, enzyme ID EC 3.4.21.26), has been identified as novel vaccine target for Chagas [12]. TcPOP is expressed in both the extracellular blood trypomastigote and the replicative intracellular amastigote [13]. It degrades collagen and fibronectin extra-cellular matrix components on host cells, facilitating parasite invasion. Its secretion into the blood during invasion, expression throughout the mammalian stages of the life cycle, and the more than 98–99% sequence conservation across DTUs [12] makes it an ideal candidate for vaccine development. This has been further supported in a murine model, as polyclonal antibodies against recombinant TcPOP, produced in *E. coli*, protected the mice from a lethal dose of the parasite [12]. *T. cruzi* triggers a complex immune response in humans, involving both innate and adaptive systems. Initially, the innate response is activated, including cytokine production by phagocytes and natural killer cells, which produce interferon-gamma [14]. The adaptive response involves T and B lymphocytes, with T cells orchestrating cellular immunity and B cells producing antibodies, although these are often ineffective due to the parasite's evasion strategies [15]. *T. cruzi* employs mechanisms including hijacking of the TGF-β signalling pathway and modulating immune responses to evade detection and establish a chronic infection. Achieving a potent and protective humoral response would be an ideal approach to block transmission in humans [16].

No structure of parasite prolyl oligopeptidases (POPs) exists to date, despite POPs being reported in *Leishmania infantum (*LiPOP*,[17])*, *Trypanosoma brucei (*Tb*POP)*[18] and *Schistosoma mansoni (*SmPOP*)*[19]. The POP family is widely distributed across Eukaryotes and Prokayotes [20]. The closest protein homologues to TcPOP for which experimental structures are available are from *Haliotis discus hannai* (PDB code 6JCI), porcine muscle POP (PDB code 1QFM), *Pyrococcus furiosus* (PDB code 5T88) and Human POP (PDB 3DDU). Comparative homology modelling studies of TcPOP have been based on porcine POP[21] and predict a cylindrical-shaped structure, consisting of a peptidase domain and a seven-bladed β-propeller domain with the substrate binding site and the canonical Asp, Ser, His catalytic triad located in the middle of the two domains [22].

The TcPOP sequence is highly similar to LiPOP (63%), TbPOP (73%) and HuPOP (43%). We therefore also expressed these other POPs and immunised mice against TcPOP to investigate cross-reactivity related to epitope conservation across species. Polyclonal antibodies (pAbs) were isolated and characterised from mice and showed striking parasite neutralising properties in cell-invasion

assays. Additionally, one monoclonal antibody was also identified from the mice exhibiting a neutralising response. The structure of TcPOP was solved by cryo-EM in closed and open conformations, revealing unexpected details on its dynamicity, corroborated by a plethora of in solution biophysical and structural techniques, which offers insights into the dynamicity of TcPOP,paving the way for new therapeutic interventions against Chagas disease.

MATERIALS AND METHODS

Bioinformatic analysis of TcPOP and TcPOP homologues

Protein sequences were extracted from the Uniprot database [23] for TcPOP (Q71MD6), TbPOP (Q38AG2), LiPOP (A4ICB5) and HuPOP (P48147) and aligned in BLASTP [24] to retrieve the top 100 homologues of TcPOP and a phylogenetic tree was built in iTOL [25] after MSA generation in MUSCLE [26]. Comparative homology models were obtained with SWISS-MODEL [27] and when it became available to the scientific community, AlphaFold2 was used to obtain AI-based models [28]. Phylogenetic analysis and sequence conservation mapping on TcPOP was done using CONSURF [29]. The topology diagram of TcPOP was created using PDBsum [30]. Geometry of the models was assessed with MOLPROBITY [31] and 3D alignment performed in PyMOL [32].

Expression and purification of POPs by bacterial fermentation

The codon-optimised genes encoding for TcPOP and orthologues were purchased from TWIST and inserted in the pET28(a)+ vector (Novagen). The resulting N-ter and C-ter His_6-tagged proteins were all recombinantly expressed and purified from the *E. coli* NiCo21(DE3) strain (NEB). Cells were grown at 37°C supplemented with 2XYT medium (Melford) until OD_{600nm} at 0.6-0.8 was reached. Protein expression was induced using 0.5 mM 1-thio-β-D-galactopyranoside (IPTG, Generon) using an 8L *in-situ* bioreactor (INFORS – Techfors S) at 100 rpm, for 18 hrs at 20°C with pH control at 7.0 (+/- 0.1), resulting in 16 grams of bacterial cell pellet. Lysis was performed using BugBuster (Nalgene) and lysate was clarified by spinning at 50,000xg for 30 min at 4°C. Affinity chromatography was performed using Co^{+2}-NTA resin (Thermo Fisher). Washing buffer (50 mM sodium phosphate, 500 mM NaCl, 30 mM imidazole, pH 7.4) and elution buffer (50 mM sodium phosphate, 500 mM NaCl, 500 mM imidazole, pH 7.4) were used during affinity purification, followed by dialysis with 3.5 kDa MWCO Dialysis membranes (Thermo Fisher) at 4°C for 18 hrs against 20 mM Hepes and 150 mM NaCl, pH 7.4. Finally, the proteins were concentrated using 30 kDa MWCO Amicon (Millipore) ultra-centrifugal filters to 10 mg/mL and immediately injected into gel filtration column S200 10/300 (Cytiva) equilibrated with 20 mM Hepes and 150 mM NaCl, pH 7.4. Elution fractions containing protein were pooled for further characterisation.

152
153
154 **Western blot analysis**
155 Samples were assessed on the SDS-PAGE gel (Bolt™ Bis-Tris Plus Mini Protein Gels, 4-12%
156 gradient) (Page Ruler Pre-stained Ladder, ThermoFisher) and transferred to nitrocellulose membrane
157 using the Trans-Blot Turbo system (Biorad). Nitrocellulose membrane was incubated with His_6-tagged
158 Monoclonal Antibody - HRP (Invitrogen) with 1:3000 v/v dilution in PBS-T, followed by the signal
159 detection using SuperSignal West Pico PLUS Chemiluminescent Substrate (Cat. 34580,
160 ThermoFisher) in an iBright system (Thermo Fisher).
161
162 **Differential scanning fluorimetry**
163 Stability measurement of prolyl oligopeptidases was carried out using a fluorescence assisted thermal
164 unfolding assay. A fluorescence stain SYPRO Orange dye solution (ThermoFisher) was used and
165 diluted to 5x concentration in 20 mM Hepes and 150 mM NaCl, pH 7.4. The assay was performed
166 with a final protein concentration of 1 μM in a total volume of 20 μL. The temperature of the protein
167 samples was gradually increased from 25°C to 95°C at a rate of 5°C per min, using the Rotor-Gene
168 Q (Qiagen). Lastly, the data were analysed using non-linear regression method to determine the
169 midpoint temperatures (T_m) of the thermal shift.
170
171 **Enzymatic tests for POPs**
172 Fluorogenic POP substrate Suc-Gly-Pro-Leu-Gly-Pro-7-amido-4-methylcoumarin (AMC)
173 (HANGZHOU JHECHEM CO LTD) was diluted in PBS to 1-25 μM final concentrations in 96-well
174 plates (ThermoFisher) to measure enzyme activity parameters in real time, with end-point reactions
175 at 10 and 30 mins, using a Gen5™ Microplate Reader and Imager Software. Stock solutions were
176 made in PBS and stored in aliquots at –20°C. The microplate readings were performed at excitation
177 360/40 nm and emission 460/40nm using BioTek Synergy LX Multimode plate reader.
178
179 **Mice immunisations**
180 The conducted animal research strictly conformed to the standards delineated by the Federation of
181 European Laboratory Animal Science Associations (FELASA). Ethical clearance for the experimental
182 methodologies was granted by the Danish Animal Experiment Inspectorate, as indicated by their
183 approval number 2018-15-0201-01541. For the purpose of immunization, female BALB/c ByJR mice,
184 aged six weeks, were obtained from Janvier Labs. Three mice were immunized intramuscularly with
185 20 μg TcPOP, emulsified in 50% v/v AddaVax adjuvant (InvivoGen). This was followed by two
186 additional intramuscular injections at biweekly intervals. A concluding intraperitoneal injection of 20
187 μg TcPOP in PBS was carried out two weeks post the last boost. Three days after the final injection,

188 the mice were humanely euthanized for the extraction of spleen and blood from which sera were
189 subsequently obtained.
190
191 **Production, purification and conjugation of anti-TcPOP mAbs**
192 After picking the best immune responders, hybridoma cell lines were generated by fusing splenocytes
193 of immunized mice with myeloma cells (ClonaCell-HY hybridoma cloning kit)[33]. Hybridoma cell lines
194 were harvested 14 days after the fusion and plated into 96-well culture plates in HT supplemented
195 media. Screening of hybridoma cell lines producing antibodies specific to TcPOP was performed by
196 ELISA, as described below. Monoclonal TcPOP-specific hybridoma cell lines were obtained by single
197 cell sorting using the FACSMelody (BD). For large-scale mAb production, hybridoma cell lines were
198 cultured in 4x250 mL cell culture flasks (Corning) as per manufacturer's instructions. Monoclonal
199 antibodies were purified by affinity chromatography using a 5 mL protein G sepharose column (Cytiva)
200 on an ÄKTAxpress system (Cytiva). Antibodies were eluted at 0.8 mg/mL in 0.1 M glycine buffer, pH
201 2.8 and immediately neutralized with 1/10 v/v 1 M Trizma hydrochloride solution (Sigma Aldrich), pH
202 9.0 to obtain the final pH 7.4. Buffer exchange to 1 x PBS was performed using a desalting column
203 (Generon) and eluted protein was concentrated with 30 kDa MWCO Amicon (Millipore) to 20 mg/mL.
204 The 3 mAbs were specifically conjugated to HRP using an EZ-*Li*nk™ Plus Activated Peroxidase Kit
205 (ThermoFisher) and detected with ECL (Pierce) using the iBright system.
206
207 **Enzyme-*Li*nked Immunosorbent Assay (ELISA)**
208 Antibody-producing hybridoma cells against TcPOP were ascertained through Enzyme-*Li*nked
209 Immunosorbent Assay (ELISA). In summary, MaxiSorp flat-bottom 96-well ELISA plates
210 (ThermoFisher) were coated with recombinant TcPOP (2 µg/mL in PBS) overnight at 4°C under
211 shaking. Plates were there washed with PBS supplemented with 0.05% v/v Tween20 (PBS-T) and
212 blocking performed for 1 hr with casein blocking solution (Pierce). The blocking solution was then
213 removed and replaced with 50 µL of hybridoma supernatant and incubated for 1 hr at RT under
214 shaking. Plates were washed three times with PBS-T before undergoing incubation with 1:10000 v/v
215 anti-mouse IgG (γ-chain specific) for 1 hr, followed by three 5 min washes with PBS-T. The positive
216 wells were identified by adding TMB plus2 (Kementec) for 20 mins and quenched using 0.2N sulfuric
217 acid. Colorimetric and absorbance signals were measured at 450 nm. Data were analysed using
218 GraphPad (Prism).
219
220 **Biological studies**
221
222 **Cell and parasite culture**
223 COLO-N680 cells (human oesophageal squamous cell carcinoma line) were maintained in complete
224 MEM medium, consisting of Minimal Essential Medium (Sigma) supplemented with 5% (v/v) heat-

225 inactivated foetal bovine serum (hiFBS, Cytiva), 100 U/ml penicillin, and 100 µg/ml streptomycin. Cells
226 were incubated at 37°C in a 5% CO_2 atmosphere and sub-cultured every 3 days at a 1:5 ratio. COLO-
227 N680 cells were seeded in complete MEM at 80-90% confluency in T25 vented flasks and infected
228 with 2×10^6 Tissue Culture Trypomastigotes (TCTs) derived from previously infected cells. Infected
229 cultures were maintained for 5 days post-infection. Free-swimming TCTs were isolated by collecting
230 and centrifuging the culture medium at 1600xg. The resulting pellets were resuspended in Dulbecco's
231 Modified Eagle Medium (DMEM) containing 5% hiFBS and maintained at 37°C for up to 4 hrs before
232 use. Motile trypomastigotes were quantified using a hemacytometer.
233
234 ***In vitro* neutralization cell-based invasion assay**
235 Trypomastigotes obtained as above were incubated in plain DMEM for at least 30 mins before starting
236 the assays. Then parasites were pelleted and incubated in DMEM prepared with the sera or
237 monoclonal antibody suspension, according to the concentration assayed. They were incubated for 4
238 hrs at 37ºC in an orbital shaker, unless specified differently. Then parasites were washed twice in
239 DMEM to remove the sera/antibodies from the medium and resuspended in DMEM prior to infection.
240 Cells were infected at a multiplicity of infection of 10:1 (parasite:cell). After 4 hrs of infection, cells
241 were washed three times with PBS to remove non-internalized parasites and incubated with fresh
242 complete MEM for 72 hrs to allow intracellular amastigote replication. Then cells were stained with 5
243 µg/ml of Hoechst and live images were acquired using an inverted Nikon Eclipse T2i epifluorescence
244 microscope. Infected cells were detached using 1 mL TrypLE Express (Gibco™) for 12 mins at 37°C
245 and fixed with 4% paraformaldehyde (PFA) for 1 hr. Cells were then washed in PBS by centrifugation
246 and resuspended in flow cytometry staining buffer (FCSB) and flowed in an Attune NxT Flow
247 Cytometer (Thermo Fisher). Gating was performed using a non-infected culture as a control.
248
249 **Immunofluorescence assays**
250 For the live binding assays, parasites were immediately fixed with 4% (v/v) formaldehyde for 1 hour
251 at room temperature following the indicated incubation time with antisera or monoclonal antibody
252 suspensions. Fixed parasites were washed twice with phosphate-buffered saline (PBS) and allowed
253 to settle by gravity onto 10-well slides for immunofluorescence (MP Biomedicals™). Parasites were
254 then permeabilized and blocked in 0.5% saponin containing 10% donkey serum in PBS for a minimum
255 of 1 hour, followed by three washes with PBS, each for 5 minutes. For classic immunostaining, where
256 parasites were directly fixed after isolation from culture, an additional incubation step was performed:
257 parasites were incubated at room temperature for 3 hours with either a 1:50 dilution of polyclonal
258 mouse antiserum or a suspension of monoclonal antibody at 1000 µg/ml in 0.5% saponin containing
259 1% donkey serum in PBS. After three washes with PBS, each for 5 minutes with agitation, parasites
260 were incubated with a secondary goat anti-mouse antibody (Alexa Fluor 488, Invitrogen) for 1 hour at
261 room temperature, protected from light. Slides underwent a final series of three washes with PBS,

262 each for 5 minutes, and were then allowed to air-dry. Finally, slides were mounted using Vectashield
263 containing DAPI for DNA staining. Images were acquired using an inverted Nikon Eclipse T2i
264 epifluorescence microscope and processed using the NIS-Nikon software.
265
266 **Biophysical studies**
267
268 **Binding kinetics of TcPOP and anti-TcPOP mAbs using biolayer interferometry**
269 Binding of anti-TcPOP mAbs to TcPOP were measured by kinetic experiments carried out on an Octet
270 R4 (Sartorius). All samples were buffer exchanged into Sartorius Kinetics Buffer, according to the
271 manufacturer's instructions. All measurements were performed at 200 µL per well in Sartorius kinetic
272 buffer at 25°C in 96-well black plates (Greiner Bio-One, Cat# 655209). ProG (Cat. Nos. 18-5082, 18-
273 5083, 18-5084) were used to immobilize anti-TcPOP mAbs for 1800s. Immunogens were four-fold
274 serially diluted in kinetic buffer in the range of 64 nM to 4 nM. Assays were performed in three
275 sequential steps with Octet BLI Discovery 12.2.2.20 software (Sartorius): Step 1, biosensor hydration
276 and equilibration (300s); Step 2, immobilization of anti-TcPOP IgG1 mAbs on a ProG biosensor
277 (600s); Step 3, wash and establish baseline (60s); Step 4, measure TcPOP association kinetics
278 (1800s); and Step 5, measure TcPOP dissociation kinetics (600s). The acquired raw data for the
279 binding of anti-TcPOP mAbs with TcPOP were processed and globally fitted to a 1:1 binding model.
280 Binding kinetics measurements were conducted in triplicate, and reported values represent the
281 average. Data were analysed using Octet Analysis Studio 12.2.2.26 Software (Sartorius) and graphs
282 produced using GraphPad (Prism).
283
284 **Epitope binning studies using Bio-layer interferometry (BLI)**
285 Anti-TcPOP mAb2 and anti-TcPOP mAb3 were applied sequentially to assess competition using the
286 BLI. Assays were performed in seven sequential steps with Octet® BLI Discovery 12.2.2.20 software
287 (Sartorius): Step 1, biosensor hydration and equilibration (300s); Step 2, immobilization of TcPOP
288 NiNTA biosensors (600s); Step 3, wash and establish baseline (60s); Step 4, measure anti-TcPOP
289 mAb2 association kinetics (1800s); Step 5, measure anti-TcPOP mAb2 dissociation kinetics (600s);
290 Step 6, measure anti-TcPOP mAb3 association kinetics (1800s); and Step 7, measure anti-TcPOP
291 mAb3 dissociation kinetics (600s). The acquired raw data for the binding of anti-TcPOP mAbs with
292 TcPOP were processed and globally fitted to a 1:1 binding model with Octet Analysis Studio 12.2.2.26
293 Software (Sartorius). The binding kinetics measurements were carried out in three replicates. Values
294 reported are the average among triplicates.
295
296 **Estimation of apo-TcPOP using SAXS**
297 SAXS was performed at the B21 beamline (Diamond *Li*ght Source, Oxon, UK). TcPOP was buffer
298 exchanged into 20 mM HEPES and 150 mM NaCl (pH 7.4) at 277K before data collection. Using an

Agilent 1200 HPLC system, 50 µL of TcPOP at 8 mg/mL was loaded onto a superdex S200 3.2/300 column for SEC-SAXS. Also, static-SAXS was performed separately at different concentrations extrapolated to zero (from 6 mg/ml to 0 mg/ml, i.e buffer condition). For SEC-SAXS, X-ray intensity data were collected as the eluent moved from the column to the beam at a flow rate of 0.16 mL/min to collect 600 frames at 3 sec intervals, while static SAXS samples were exposed to X-rays to collect 21 frames at 1 sec time intervals. The intensity was plotted against its angular dependants q ($q = 4\pi\sin\theta/\lambda$) while, the system operated with an exposure time of 3 sec at 12.4 keV (1Å) using a EIGER 4 M detector. Data were analyzed using the BioXTAS RAW [34], ATSAS program suites [35], DENNS[36] and plotted using GNOM[37].

Mass photometry

Buffer optimisation for TcPOP

Mass photometry (MP) experiments were conducted using the Refeyn OneMP mass photometer, after cleaning coverslips and gaskets with 100% isopropanol and water. Measurements, performed in triplicate, involved systematic optimizations of pH values in the range 7.0-8.0 and with NaCl concentration range 50-300mM within a 20 mM BTP buffer. Protein was diluted in buffer to a final concentration of 120 nM into a gasket well, followed by focal point acquisition and data analysis using Refeyn AcquireMP 2.3.1 software. MP movies (6000 frames, 20 frames per sec) were captured within a 10.8 × 10.8 µm field and processed with Refeyn DiscoverMP 2.3.0 software. Robust data analysis ensued, leveraging a contrast-to-mass (C2M) calibration approach. Calibration involved introducing 3 µL of a 1:100 v/v pre-diluted NativeMark standard (LC0725, Thermo Scientific) to an acquisition well, yielding masses (66, 146, 480, 1048 kDa) that informed the calibration curve employed in DiscoverMP software. Experiments were performed at the Leicester Institute for Structural and Chemical Biology (LISCB, University of Leicester, UK).

Anti-TcPOP binding measurements

MP measurements were conducted using a Refeyn TwoMP (Refeyn Ltd) as previously described [38]. Briefly, glass coverslips (High Precision No. 1.5H, Marienfeld Superior) were cleaned by sequential sonication with Milli-Q H_2O, 50% isopropanol and again Milli-Q H_2O. Cleaned coverslips were dried using nitrogen flow. CultureWell™ reusable gaskets (3 mm diameter x 1 mm depth, Grace Bio-Labs) were used to assemble sample chambers. Coverslips were placed on the MP sample stage and a single gasket was filled with 20 µL DPBS (wo/ calcium and magnesium, pH 7.4, ThermoFisher Scientific) to find focus. TcPOP, mAb1, mAb2 and mAb3 were measured separately at a final concentration of 20 nM. For TcPOP-antibody binding assays, 5 µM TcPOP was mixed with 5 µM mAb2 or mAb3 in a 1.5 mL Eppendorf tube at a 1:1 v/v ratio. The sample mixture was equilibrated for 10 mins and diluted 1:100 before data acquisition. Acquisition settings were adjusted within AcquireMP

336 (2023 R1.1, Refeyn Ltd) as a large field of view, frame binning = 2, frame rate = 128.2 Hz, pixel binning
337 = 6, exposure time = 7.65 ms. Movies were taken over 60 sec. Mass calibration was performed using
338 an in-house protein standard including 90-720 kDa oligomers. Data were analysed and histograms
339 were created with Discover MP (v2023 R1.2, Refeyn Ltd). Experiments were performed at the New
340 Biochemistry building (University of Oxford, UK).
341
342 **MD simulations**
343 Atomics coordinates of TcPOP were retrieved from the AlphaFold database. To calculate the
344 conformational dynamics of TcPOP, all-atom molecular dynamics simulations were conducted on an
345 Ada High Performance Computer (HPC, University of Nottingham) using the GROMACS 2021.2-
346 fosscuda-2020b package. GROMOS 54a7 forefield was applied and hydrogen atoms were
347 incorporated using the pdb2gmx module, and topology files were generated under periodic boundary
348 conditions (PBC) employing a cubic periodic cell. The protein was centrally placed, solvated using
349 simple point charge (SPC) 216 water molecules and positioned 1 nm from the edges, with NaCl
350 counter ions added for system neutralization.
351 Following energy minimization, the canonical ensemble (NVT) underwent equilibration for 100 psec
352 without pressure coupling and Berendsen thermostat was initially applied. Subsequently, temperature
353 (298 K) was maintained by velocity rescaling with a stochastic term, while the isothermal-isobaric
354 ensemble (NPT) with a 1 bar pressure for 100 psec, using the Parrinello–Rahman method, was
355 implemented. The LINCS algorithm constrained H-bonds, and the MD simulations ran for 500 nsec
356 with a 2-fs time step. The resulting trajectory was analysed using inbuilt functions of the GROMACS
357 package[39].
358
359 **Cryo-EM sample preparation, data collection and processing**
360
361 **Cryo-EM grid preparation**
362 Homogeneous samples from SEC purified in 20 mM HEPES, 150 mM NaCl, pH 7.4 were freshly used
363 to prepare the grids. Fraction corresponding to the SEC peak at 15 mL (Fig.S2) was used at a final
364 concentration of 0.2 mg/mL. Firstly, cryoEM grids, R1.2/1.3 carbon, Au 300 (Quantifoil), were glow
365 discharged in the presence of amylamine for 30 sec at 10 mA on a Quorum GloQube glow-discharge
366 unit. Four microliters of the freshly prepared TcPOP sample were applied to the grid and blotted for 3
367 sec, with blot force 10, prior to flash-cooling in liquid ethane using a Vitrobot Mark IV (FEI
368 ThermoFisher), set at 4 °C and 100% humidity.
369
370 **CryoEM data collection**
371 CryoEM grids were imaged using a 300 KeV Titan Krios G3 (ThermoFisher Scientific) transmission
372 electron microscope (Midlands Regional Cryo-EM Facility, University of Leicester) at a calibrated pixel

size of 0.656 Å. Electron micrographs were recorded using a K3/GIF (Gatan Imaging Filter) direct electron detector (Gatan Inc.) and EPU automated data acquisition software (ThermoFisher Scientific). Micrograph movies were recorded with 75 fractions, in super resolution, binned by 2 and a total dose of 77 e^-/pix (dose rate of 15 e-/pix/s), To improve the distribution of particle views, data were collected at 0°, 30° and 35°. At 0° tilt (Dataset 1), the defocus range was collected between -2.3 and -0.8 µm, in regular intervals. At 30° and 35° tilt (Dataset 2), the defocus was set to -1.2 µm.

Cryo-EM image processing

Image processing was carried out on the cryo-EM computational cluster at the University of Leicester. Micrographs were pre-processed using Relion5-beta,[40] sample motion during acquisition was corrected using RELION's own implementation, Dataset 2 was dose-weighted, Dataset 1 was not. Micrographs were then CTF estimated using CTFFIND4.1[41]. Initially each dataset (i.e. 0° tilt, 30° tilt and 35°) was processed separately. In brief, particles were picked using Topaz[42], then extracted with a box size – 256pixels (corresponding to 168Å) binned by 4 to 2.624 Å/pix. Particles were filtered in 2D to produce a set of images which were then used for *ab-initio* model generation in RELION 5-beta. Analysis of the 3D initial models revealed "open" and "closed" conformations. The full set of Topaz picked particles was classified in 3D with Blush regularisation[43] and the classes were inspected and subcategorised into open and closed particles. Re-extraction of the particles at 1.312 Å/pix followed by 3D auto-refinement and CTF parameter refinement of all three datasets was then carried out. Despite having a 3DFSC sphericity > 0.9, The 0° tilt dataset showed severe preferential orientation and concomitant overestimation of resolution and B-factor parameters was observed. All three datasets were then merged but this resulted in only marginally improved maps.

Further analysis of the 35° tilt dataset was then performed with DynaMight[44]. This showed that both the open and closed conformations had a moderate degree of continuous motion, explaining why the map quality was limited despite having a large number of high-quality particles. The consensus deformed back projection of both open and closed conformations were then calculated. Map sharpening was done with Relion's automatic B-factor estimation as well as DeepEMhancer[45].

409

Data collection and processing	Dataset 1 (untilted)	Dataset 2 (tilted)
Magnification (nominal)	130,000 x	130,000 x
Voltage (kV)	300	300
Stage (Z) tilt	0	-30 and -35
Aberration free image shift (AFIS)	Yes (12 µm)	No
Electron exposure (e^{-}/Å^{2})	76.43	77.59
Illuminated area (µm)	0.65	0.57
Fractionation	75	75
Defocus range (µm)	-2.3 to -0.8	-1.2µm
Pixel size (Å)	0.656	0.656
Total micrographs (no.)	20,080	2,292
Total particle images (no.)	45,400,101	2,525,462
Final particle images (no.)	847,560 (closed) 518,852 (open)	163,153 (closed) 126,459 (open)
AutoRefine map resolution @ 0.143	3.29Å (closed) 3.50Å (open)	4.00Å (closed) 4.10Å (open)
AutoRefine 3DFSC global resolution @ 0.143 (sphericity)	3.29Å (0.929) (closed) 3.43Å (0.908) (open)	3.82Å (0.929) (closed) 4.10Å (0.912) (open)
DynaMight map resolution @ 0.143	n/a	3.57Å (closed) 3.82Å (open)
DynaMight 3DFSC global resolution @ 0.143 (sphericity)	n/a	3.52Å (0.960) (closed) 3.93Å (0.964) (open)
Initial model used	*Ab initio*	*Ab initio*

410 Table 1 Cryo-EM data collection, refinement and validation statistics

411

412 **Cryo-EM model fitting and refinement.**

413 The coordinates of the open and closed conformations of TcPOP were docked in the respective cryo-
414 EM maps using phenix.*dock_in_map*[46]. Both maps were refined in PHENIX using real space
415 refinement with 3 cycles of simulated annealing (SA), followed by re-build in place and 10 cycles of
416 refinement at each SA step. Model building was performed in COOT[47]. Structures were validated
417 using the Molprobity tool, as implemented in PHENIX. ChimeraX[48] was used to generate visual

418 molecular graphics. The FSC of the closed and open CryoEM maps were calculated using EBML-EBI
419 FSC-server[49]. Cryo-EM reconstructions have been deposited in the EM Data Bank (EMDB).

420

421 ***Plasmonic Optical nanotweezers: samples preparation and data collection***

422 We used a plasmonic optical tweezers setup which is a modified modular optical tweezers system
423 (OTKB/M, Thorlabs) in the Advanced Optics and Photonics Lab at Nottingham Trent University
424 (Nottingham, UK) with a 852 nm Fabry-Perot laser diode (FPL852S, Thorlabs)[50]. The laser beam was
425 polarised perpendicular to the centre-to-centre line of two circles of the double nanohole (DNH)
426 structure by using a polariser and a half-wave plate and was collimated and focused on the DNH by
427 a 60X air objective (NA 0.85, Nikon). All trappings were performed at a laser power of 25 mW[51] The
428 transmitted laser intensity was then converted to a voltage signal via a silicon avalanche photodiode
429 (APD120A, Thorlabs) and recorded by a data acquisition card with a sampling rate of 1 MHz. The
430 recorded voltage data (transmission traces) were normalised and filtered using in-house MATLAB
431 scripts, which included a zero-phase Gaussian low-pass filter (MATLAB *filtfilt.m*) with cut-off
432 frequencies of 10 kHz, 1 kHz, 100 Hz, and 10 Hz. Probability density function (PDF) was calculated
433 by using MATLAB function *ksdensity.m*. More information on this specific set-up have been previously
434 reported[52]. SEC Purified TcPOP was used at 1 μM concentration in PBS. DNHs were sealed into the
435 flow cell using cover glass with a double-sided tape as a spacer, providing a microfluidic channel with
436 3.5 μL volume. The solution was delivered to the flow cell using a 12-way valve and a syringe pump.
437 Initially, TcPOP was infused in the chamber to achieve trapping followed by the sequential infusions
438 of 1 μM, 10 μM and 100 μM substrate Suc-Gly-Pro-Leu-Gly-Pro-AMC to the flow cell at a flow rate of
439 2 μL/min.

440

441 **Hydrogen-deuterium exchange (HDX) mass spectrometry (MS)**

442 Prior to conducting HDX-MS experiments, peptides were identified by digesting TcPOP using the
443 same protocol and identical liquid chromatographic (LC) gradient as detailed below and performing
444 MS^E analysis with a Synapt G2-Si mass spectrometer (Waters), applying collision energy ramping
445 from 20 to 30 kV. Sodium iodide was used for calibration and leucine enkephalin was applied for mass
446 accuracy correction. MS^E runs were analysed with ProteinLynx Global Server (PLGS) 3.0 (Waters)
447 and peptides identified in 3 out of 4 runs, with at least 0.2 fragments per amino acid (at least 2
448 fragments in total) and at least 1 consecutive product, with mass error below 7 ppm were selected in
449 DynamX 3.0 (Waters).

450

451 For the continuous deuterium labelling (HDX), TcPOP (48 μM) was diluted 1:50 in a deuterated buffer
452 at 20 mM HEPES, 150 mM NaCl (96.5% D_2O fraction, pH_{read} 7.0) and the exchange reaction was
453 conducted for 2 sec, 10 sec, 100 sec, 1,000 sec, 10,000 sec and 18 hrs at room temperature. The

exchange reactions were quenched by a 1:1 dilution into ice-cold 100 mM phosphate buffer containing 3 M urea and 70 mM tris(2-carboxyethyl) phosphine (TCEP) (final pH_{read} 2.3). Samples were held on ice for 30 sec, snap-frozen in liquid nitrogen and kept frozen at –80°C until LC-MS analysis. A maximally labelled sample (MaxD) was produced by labelling TcPOP with 3 M fully deuterated urea in D_2O and 2.5 mM TCEP, resulting in a final deuterium content as for the other labelled samples. The maximally labelled sample was quenched after 16 hrs by 1:1 v/v dilution into ice-cold 100 mM phosphate buffer (final pH_{read} 2.3), held for 30 sec on ice, snap-frozen in liquid nitrogen and kept frozen at -80°C until LC-MS analysis. A pulse labelling experiment (two technical replicates) was conducted to assess the protein stability and rule out irreversible unfolding of the protein over time. An aliquot of TcPOP was quickly unthawed and immediately labelled for 10 sec, then exposed to room temperature on the bench for 10,000 sec (as under conditions of continuous labelling) and labelled again for 10 sec. Frozen protein samples were quickly thawed and injected into an Acquity UPLC M-Class System with HDX Technology (Waters). The protein was on-line digested at 20°C into a home-made pepsin column and trapped/desalted with solvent A (0.23% formic acid in water, pH 2.5) for 3 min at 200 µL/min and at 1 °C through an Acquity BEH C18 VanGuard pre-column (1.7 µm, 2.1 mm × 5 mm, Waters). Peptides were eluted into an Acquity UPLC BEH C18 analytical column (1.7 µm, 2.1 mm × 100 mm, Waters) with a 7 min-linear gradient raising from 8 to 35% of solvent B (0.23% formic acid in acetonitrile) at a flow rate of 40 µL/min and at 1 °C. Then, peptides went through electrospray ionization in positive mode and underwent MS analysis with ion mobility separation.

Peptide level deuterium uptake was calculated with DynamX 3.0 (Waters) and data visually inspected and curated. Selected peptides exhibiting evident bimodal HDX behaviour (a clear sign of correlated exchange) were analysed by HX-Express3[53] (HX-Express Software). Binomial fitting was applied with optimized fits for the number of amides, and undeuterated mass envelopes were calculated from the peptide sequence and fitted into the experimental undeuterated mass envelope to check the agreement. Subsequently, bimodal deconvolution (double binomial) was enabled for mass envelopes flagged as bimodal. The relative deuterium uptake (Da) and population fraction of both low- and high-mass envelopes were calculated. The fraction of the high-mass population (*y*) over the time points studied (*x*) was subjected to single or double exponential fitting by HX-Express3 to calculate the kinetic parameter Kop (rate of opening), according to the following exponential function:

$$y = start\ fraction + [weight\ fraction\ \times (1 - exp^{-Kop \times x})]$$

To determine the number of backbone amide hydrogens undergoing correlated exchange (#NHs) for the individual peptides, the time point showing maximal difference in HDX between the low- and high-mass population (Max ΔHDX) was identified. Then, the Max ΔHDX value was normalized by the

490 peptide MaxD uptake and corrected for the number of exchangeable amides (N) and D_2O fraction (=
491 0.9457), according to the following equation, as previously described[54,55]:
492
493 $$NHs = \frac{Max\ \Delta HDX}{MaxD\ uptake} \times N \times D_{fraction}$$ [i]
494
495

496 # Results

497 **Expression and purification of TcPOP and TcPOP homologues**

498 Prolyl oligopeptidases (POPs) belong to the large hydrolase family, which is highly conserved in
499 eukaryotes. To explore the evolutionary and functional similarities, we compared *T. cruzi POP*
500 (TcPOP) to two close parasite homologues, namely those in *T. brucei* (TbPOP), *L. infantum* (LiPOP),
501 and to the *Homo sapiens* homologue (HuPOP). Phylogenetic analysis and sequence conservation
502 mapping on TcPOP highlighted that conserved and variable regions are located in both the catalytic
503 and non-catalytic domains (Fig.S1a). Notably, the AlphaFold3 modelling of collagen binding to TcPOP
504 corroborated previous docking studies with the substrate-binding site at the interface of the two
505 domains (Video S1). This is a region of high variability, as indicated by the phylogenetic analysis
506 (Fig.S1b). [22] TcPOP was expressed in *E. coli* using bacterial fermentation, overcoming the challenge
507 of extremely low expression yields in batch culture (~ 0.05 mg/L) (Fig. 1a). In contrast, expression of
508 the other homologue proteins led to higher protein yields (0.8-2.0 mg/mL) (Fig.S2a). Following
509 purification by size-exclusion chromatography (SEC) (Fig. S2b), all POPs exhibited enzymatic activity
510 (Fig. S3a–c), thermostability, as determined by differential scanning fluorimetry (DSF) (Fig. S3d), and
511 comparable end-point kinetics consistent with previously reported values for this enzyme family[56].
512 SEC-MALS analysis confirmed that all proteins were monomeric and monodisperse in solution
513 (Fig.1b) and predicted the expected mass within the experimental error of the technique (TcPOP:
514 73.4 (±2.1%) kDa, TbPOP: 73.7 (±1.6%) kDa, LiPOP: 75.7 (±3.5%) kDa, HuPOP: 85.3 (±1.71%) kDa)
515 (Fig. S4a). AlphaFold3 modelling of TcPOP predicted a structure comprising an α/β-hydrolase domain
516 housing the catalytic triad Ser548-Asp631-His667, and a seven-bladed beta-propeller non-catalytic
517 domain (Fig. S5), consistent with the previously determined structure of porcine POP (PDB code
518 1QFM)[22].

519 **Anti-TcPOP polyclonal response is cross-reactive**

520 To assess the cross-reactivity of antibodies raised against TcPOP, mice were immunized with the
521 recombinant enzyme. Homologous proteins with high amino acid identity from *L. infantum* (LiPOP,

522 63%), *T. brucei* (TbPOP, 73%), and *H. sapiens* (HuPOP, 43%) were expressed and purified to
523 evaluate potential cross-reactivity, driven by the likelihood of shared epitopes (Fig.S1a). Three mice
524 were immunised with TcPOP and polyclonal response analysed by ELISA (Fig.1c). The
525 corresponding TcPOP-specific sera were tested against all four POPs. Cross-reactivity was detected
526 to TcPOP, TbPOP, and LiPOP, but not for HuPOP at serially diluted serum concentrations. These
527 findings suggest potential epitope conservation across parasite species, but not with HuPOP (Fig.
528 S6a).

529 **Anti-TcPOP polyclonal sera block parasite invasion**

530 To evaluate the neutralizing properties of anti-TcPOP polyclonal sera, we adapted our trypomastigote
531 drug screening procedure [57] to a cell-based invasion assay (Fig.1d). Polyclonal antisera from all three
532 mice demonstrated significant neutralizing activity, greatly reducing trypomastigote invasion of COLO-
533 N680 cells compared to the naïve serum and serum derived from mice chronically infected with *T.*
534 *cruzi.* (Fig. SS7a). Overall, we found that all three independently derived sera achieved a >95%
535 neutralising effect, an impact that approached 99% for the serum from mice 1 (IM1S (Fig.1e-f), as
536 measured by flow cytometry 72 hrs post infection (Supplementary Fig. S8a-b). The potency of IM1S
537 was maintained even when reduced to 2.5% (Fig. 2a-b and Fig. S7b).

538 Immunofluorescence analysis of freshly extracted and fixed parasites revealed that the anti-TcPOP
539 antisera bound in the endocytic/exocytic pathway of trypomastigotes (Fig. 2c, Supplementary Fig.
540 S9b and Video S2). This pattern differed from antiserum from chronically infected mice, which
541 showed the expected dispersed binding on the parasite surface, associated with a non-protective
542 response (Fig. 2c). To understand the dynamics of IMIS binding, we performed a real-time assay
543 which revealed that antibody attachment led to parasite lysis within minutes. To dissect this effect, we
544 monitored the process by reducing the amount of serum and decreasing the temperature from 37ºC
545 to 30ºC. (Fig. 2d, Supplementary Fig. S9a). Even under these constrained conditions, parasites
546 became swollen after 5 mins exposure, followed by intracellular leakage and parasite lysis within 15
547 mins. (Fig. 2e, Supplementary Fig. S9c). To confirm this lytic effect, we incorporated a competition
548 assay, including foetal bovine serum (FBS) at the same concentration as the IM1S. At the early
549 timepoints, parasite integrity was preserved, and the majority of binding was restricted to the parasite
550 surface. (Supplementary Fig. S9d).

551 Additionally, we investigated binding to amastigotes, the intracellular form of the parasite. This life-
552 cycle stage is also infectious, for example, when are released as host cells rupture following
553 trypomastigote egress. The amastigote binding profile also highlighted the endocytic/exocytic
554 pathway (Supplementary Fig. S9b). However, in live-binding assays, we also observed that surface
555 attachment of anti-TcPOP, located at the apical end of the amastigote (Supplementary Fig. S9c-d).

556 Finally, we determined binding in epimastigotes, the replicative insect form of the parasite The main
557 location was at the anterior end, adjacent to the cytostome-cytopharynx complex, an additional
558 secretory portal found in this form of the parasite. (Supplementary Fig. S9c-d). Overall, the binding
559 studies reveal that TcPOP antisera is associated predominantly with the secretory pathway in all
560 forms of the parasite.

561 **Anti-TcPOP monoclonal response**

562 Three anti-TcPOP monoclonal antibodies (mAbs) were generated from the spleen of the mouse with
563 the highest polyclonal serum response (Fig.3a) and screened by ELISA for specificity against TcPOP
564 (Fig.3b) and homologue POPs (Fig.S6b). TcPOP antibody titres were positive at 1 µg/ml for mAb1
565 and at 0.1 µg/ml for mAbs 2 and 3 (Fig.3b), while no binding was observed against LiPOP, TbPOP
566 and HuPOP. HRP-conjugation of anti-TcPOP mAbs revealed the presence of both linear and
567 conformational epitopes, as confirmed by Western blot analysis (Fig. 3c).
568
569 The BLI-based binding profile for immobilised anti-TcPOP mAbs against TcPOP showed higher
570 binding affinity to TcPOP for anti-TcPOP mAb2 (K_D <1 pM, K_a (1/Ms) 2.3 x 10^5, K_{diss} (1/s) < 10^{-7}) and
571 anti-TcPOP mAb3 (K_D <1 pM, K_a (1/Ms) 3.1 x 10^5, K_{diss} (1/s) < 10^{-7}). Instead, anti-TcPOP mAb1
572 exhibited comparatively weak binding (K_D < 3.2 nM, K_a (1/Ms) 7.1 x 10^4, K_{diss} (1/s) 6.2 x 10^{-4}) (Fig. 3d),
573 as well as association and dissociation parameters. The best two mAbs, mAb2 and mAb3, were used
574 to perform a sequential affinity binding with association and dissociation length of 1800 sec and 600
575 sec respectively. Both mAbs showed detectable association and dissociation (K_D <1 pM, K_a (1/Ms)
576 >10^7, K_{diss} (1/s) < 10^{-7}) indicating competition for different epitopes (Fig.S11c).

577 Mass photometry measurements of TcPOP and the three individual anti-TcPOP mAbs, were 85 kDa
578 and 151 kDa, respectively, with only a single peak present in each MP spectrum (Fig.S11a-b).
579 Interaction studies revealed similar binding between TcPOP and both antibodies. A peak
580 corresponding to 1:1 (mAb to TcPOP) was observed at 233 kDa with a relative abundance of 1-2%
581 (TcPOP-mAb1), 17% (TcPOP-mAb2) and 19% (TcPOP-mAb3). No evidence of higher-order binding
582 was found (Fig.3d).
583
584 **Anti-TcPOP monoclonal antibody neutralises parasite invasion**

585 To further investigate the neutralising activity of the mAbs, we performed a cell-based infection assay
586 incubating the parasites in 1000 µg/ml of each purified antibody in DMEM. Notably, mAb1 caused a
587 significant reduction in parasite invasion, approaching 50% (Fig. 3f, Supplementary Fig. S10a).
588 Additionally, we found that this neutralising effect was maintained regardless of the concentration
589 assayed (Fig. 3f), and that instead of inducing a lytic effect, the effect was mediated by steric

590 hinderance resulting from the binding to the surface of the trypomastigotes (Fig. 3g). The colocation
591 assay showed a specific binding in a line along the flagellum (Supplementary Fig. S10b-c,
592 Supplementary Video S3). Additionally, we observed that in amastigotes, the binding also associated
593 with the short flagellum, that in these rounded forms of the parasite, is largely confined to the flagellar
594 pocket (Supplementary Fig. S10b-c).

595 **Determination of cryo-EM structure of TcPOP in multiple conformations**

596 **TcPOP structure determination using single particle cryo-EM**

597 We analysed the structure of TcPOP using single particle analysis (SPA) cryo-EM. 2D classification
598 highlighted equal distribution of the particles in the micrographs (Fig.S12). The initial data collection
599 comprised of 20,080 micrographs revealed severe preferential orientation[58] resulting in poor map
600 reconstructions (Fig.S13). Several approaches were attempted in cryo-EM grid preparation including
601 changes in detergent, support films and glow discharge parameters. However, none led to significant
602 improvement in the orientation distribution. We therefore tilted the grids to 30° and 35° to increase the
603 number of views visualised in the electron micrographs (Fig.S13). This significantly improved the
604 number of views, and the map produced was drastically improved with continuous density and
605 minimal anisotropic features (Fig.S13). 3D classification revealed two distinct conformations of
606 TcPOP i.e. open and closed (Fig.S13), indicating intrinsic conformational heterogeneity of the dataset.
607 Closed and open conformation models obtained from AlphaFold and homology modelling (using PDB
608 3IUJ), respectively, were then docked into their respective CryoEM maps and refined (Figure 4a-b,
609 Table 2). Local resolution was also estimated using half-maps in PHENIX (Fig. 4a-b).

Refinement parameters	**Closed conformation**	**Open conformation**
PDB entry	9HJI	9HJJ
FSC (model) (masked) = 0.143	3.57 Å	3.82 Å
Correlation Coefficient (masked)	0.7	0.7
Molprobity Score	2.42	2.54
Clash score	12.95	14.79
Ramachandran allowed	100 %	100%
Ramachandran favoured	94.39%	90.79
Ramachandran outliers	0%	0%
Poor rotamers	3.51%	2.84%
Overall B factor (isotropic)	70	90
Bad bonds (RMSD)	0%	0%
Bad angles (RMSD)	0.01%	0.01%

610 Table 2 Cryo-EM statistics for closed and open conformation from real-space refinement in PHENIX
611 [59].

612 Our cryo-EM data confirm that TcPOP comprises two distinct domains: a catalytic α/β-hydrolase
613 domain, which houses the active site featuring the catalytic triad, and a β-propeller domain, which
614 likely regulates substrate access. The spatial arrangement of these domains reveals a cylindrical
615 structure, with the β-propeller domain capping the catalytic α/β-hydrolase domain, as previously
616 postulated[60]. This configuration suggests a gating mechanism controlling substrate entry to the active
617 site, which may play a critical role in modulating enzymatic activity. These findings align with the
618 proposed role of TcPOP in hydrolysing large substrates and facilitating parasite invasion into host
619 cells.

620

621 **SAXS and mass photometry analysis**

622 SEC-SAXS profiles on purified TcPOP sample indicates no aggregation and globular conformation
623 leading to an estimated molecular weight of 73.4 kDa [61] , based on Kratky plot and Guinier analysis
624 Open and closed conformations were also de-convoluted and the corresponding cryo-EM models
625 were docked into the molecular envelopes (Fig.4c). Static SAXS data were also collected in a range
626 concentrations, including zero-concentration, to determine the optimal level for SAXS data analysis
627 and for data processing (Fig.S15). Mass photometry also allowed identification of the best buffer
628 conditions in term of ionic strength and pH values (Fig.S11a). This information was exploited for cryo-
629 EM grid preparation to increase sample homogeneity and also for buffer optimisation to elucidate
630 TcPOP-mAbs interaction in BLI.

631 **MD simulation of TcPOP**

632 To understand the intrinsic dynamicity of TcPOP, molecular dynamics simulations were performed
633 using the AlphaFold model from Uniprot (Q71MD6) as the starting point for 500 nsec simulations,
634 which showed notable transitions in Root Mean Square Deviation (RMSD) around 290 nsec, while
635 Root Mean Square Fluctuation (RMSF) (Fig.5a) and Solvent Accessible Surface Area (SASA) and
636 radius of gyration (Rg) (Fig. S16) underwent complementary contraction for the first 300 nsec,
637 followed by significant expansion up to 500 nsec, indicating substantial conformational changes.
638 RMSF analysis identified residues 192-198 and 306-333 as highly flexible. The Gibbs free energy
639 landscape analysis identified four significant minima basins, providing insights into local and global
640 minima in a 2D and 3D projection of FEL, as described previously[62] (Fig.5a).

641

642 **Plasmonic Optical nanotweezers confirms TcPOP dynamicity in solution**

643 Aperture-based plasmonic nano-tweezers revealed the conformational dynamics of single,
644 unmodified TcPOP. TcPOP trapping events were detected by changes in transmission levels, filtered
645 at a cut-off frequency of 1 kHz, whilst time traces of $\Delta T/T_0$ of TcPOP trapped in the absence of
646 substrate AMC (blue and purple, Fig.S17), and with 100 μM AMC substrate introduced to the trapping
647 site. Addition of substrate at 100 μM concentration led to larger fluctuations in transmission, indicating
648 TcPOP exhibiting greater dynamic fluctuations during enzymatic cycles than in its apo-state.
649 However, in the absence of a substrate, distinct signal fluctuations were observed above the
650 background of Brownian motions in the trapping well, suggesting free transition of multiple
651 conformations of TcPOP in solution. This is further corroborated by distinct peaks in the probability
652 density functions (PDFs) (Materials and Methods).

653 **Structural dynamic analysis of TcPOP by HDX-MS**

654 To gain insights on the kinetics of transition between the closed and open conformation in TcPOP,
655 we applied hydrogen-deuterium exchange (HDX) mass spectrometry (MS) (Table S1 in HDX
656 Supplementary data). HDX-MS enables the monitoring of the structural dynamics of proteins in
657 solution, based on the rate at which individual backbone amide hydrogens exchange with deuterium
658 atoms[63]. The two domains of TcPOP proved to be similarly dynamic, both containing regions of rapid,
659 medium, or fast HDX (Fig. 5b, and S19 and S20). Remarkably, peptides of several helices and loops
660 of the α/β-hydrolase domain and of a single loop of β-propeller domain (Fig. S18) exhibited bimodal
661 isotopic envelopes with resolved high- and low-mass distributions, whose intensities interconvert over
662 time: a clear sign of EX1 and EXx kinetics. This type of HDX behaviour is generally seen for groups
663 of amides undergoing cooperative unfolding events (correlated exchange) and populating an open
664 state for a sizeable time frame[63,64]. By pulse deuterium labelling, we established that those segments
665 are not irreversibly unfolding over time and that TcPOP is in a dynamic equilibrium under our HDX
666 conditions. Therefore, every opening event (determined by the rate constant k_{op}) is reversible (Fig.
667 S21). The bimodal isotopic envelopes were fitted[65] to determine the number of amides involved in
668 correlated exchange, the kinetic parameters k_{op}, and HDX half-life of the closed state (Figs. S22a-j
669 and S23, and Table S2 in HDX Supplementary data), which report on the relative rates at which
670 individual helices/loops of TcPOP transition to the open conformation. We localized the correlated
671 exchange at the level of the amides indicated in Fig. 5c. We observed that the loop 191-209 (β-
672 propeller domain, at the interface with the α/β-hydrolase domain) and the helix 495-521 and adjacent
673 loop 465-479 (α/β-hydrolase domain) manifest a starting open state of approximately 40% of the
674 population, indicating that these specific segments adopt two initial non-interconverting distinct

675 conformations, and subsequently very fast transition to the open state (average half-life <1,000 min
676 at 23 °C). All other regions (helix and loop spanning residues 16-48, and helix 545-608 of the α/β-
677 hydrolase domain) have an initial open state that approximates to 0%, with segment 16-48
678 interconverting very slowly to the open state (average half-life >2,000 min at 23 °C), and segment
679 545-608 interconverting at medium rate (average half-life between 1,000 and 2,000 min at 23 °C)
680 (Fig. 5c-d and S23). Taken together, our HDX-MS data corroborate with the existence of the TcPOP
681 open and closed conformations that could be resolved in cryo-EM, and with the presence of
682 intermediate conformations that arise from the switching of selected helices and loops at different
683 rates.

684

685 # Discussion

686 Structural data on *T. cruzi* antigens are desperately needed to guide vaccine development and design
687 of diagnostic solutions. Such data are invaluable to initiate structure-based immunogen design
688 strategies which focus the immune response towards key conserved epitopes[66] and to identify regions
689 within the target protein suitable for drug design. TcPOP is one of the leading validated candidates
690 for a Chagas disease vaccine, given its high level of sequence conservation across the six genotypes
691 (or DTUs) of the *T.cruzi* species.

692 The three-dimensional structure of TcPOP remained elusive for almost two decades since a
693 comparative homology model was proposed in 2005[22]. Several attempt to crystalise parasite POPs
694 in our lab, including TcPOP, LiPOP, TbPOP and HuPOP, did not succeed, despite the usage of
695 starting protein concentrations up to 500 μM for crystallisation screening (equivalent to ~ 40 mg/mL).
696 Closed conformations for TcPOP homologues have been previously reported using protein
697 crystallography from porcine POP (PDB code 1QFM), *Pyrococcus furiosus* (PDB code 5T88), or
698 HuPOP with an irreversible inhibitor (PDB code 3DDU), to lock the enzyme in the closed state.
699 However, to our knowledge, neither fully open nor fully closed conformations of a parasite POP in a
700 single solution (with or without the aid of additives) have been determined previously. High solubility
701 was a characteristic of not only TcPOP, but also of other POPs reported in this manuscript, and this
702 is likely to be linked to their function of being secreted in the blood to perform degradation of the
703 extracellular host matrix. In fact, TcPOP possess 33 Lys residues, out of which, 13 are located on
704 the solvent accessible surface, a feature that likely prevents the crystal contacts required to promote
705 crystallisation. Methods have been developed to reduce protein entropy by lysine methylation[67] but
706 we opted not to use this strategy, as this could have compromised antigenicity by altering potential
707 key residues involved in epitope-paratope interaction.

708 Immunizing mice with recombinant TcPOP led to the production of polyclonal antibodies that showed
709 cross-reactivity with *L. infantum* and *T. brucei* homologs, indicating conserved epitopes among these
710 parasites. However, the lack of response to the human homolog led to the speculation that there
711 might be a divergence in epitope conservation across species. This might be attributable to
712 evolutionary pressure or possible immune suppression in the human host, although this remains to
713 be established. Such observed cross-reactivity not only underscores the potential for developing
714 cross-protective vaccines against related parasite species but also emphasizes the precision in
715 targeting pathogen-specific epitopes, while minimizing cross-reactivity with human proteins for
716 diagnostic applications. Here, we investigated the immune response in mice at both the polyclonal
717 and monoclonal level to TcPOP. Polyclonal antibodies from all three mice exhibited striking
718 neutralization effects, approaching 100%, and leading to rapid parasite lysis of the infectious
719 trypomastigote stage. These findings consolidate TcPOP's central role as a leading candidate for a
720 Chagas disease vaccine. Additionally, the production and characterization of three monoclonal
721 antibodies from the mouse with the highest polyclonal response identified a single mAb (IM1-mAb1)
722 responsible for approximately 50% of the neutralization effects. Unexpectedly, this mAb, despite
723 being neutralising, did not induce parasite lysis, suggesting the presence of an alternative
724 neutralization mechanism, potentially involving hindrance, as indicated by cell localization
725 experiments.

726 Interestingly, the IM1-mAb1was the weakest binder *in vitro* among the three isolated mAbs, exhibiting
727 faster *kon* and *koff* rates, whilst the others exhibited much longer *koff* rates. This underscores the
728 importance of testing all mAbs in a cell-invasion scenario that more closely reflects host-pathogen
729 interactions, without excluding any based on *in vitro* studies alone, as interactions with the parasite
730 may reveal neutralizing potential.

731 In our quest to determine the three-dimensional structure of TcPOP, the AlphaFold model of the
732 closed conformation of TcPOP highlighted its dynamic nature, showing significant transitions in the
733 Cα-backbone during the course of molecular dynamics (MD) simulations. Also, MD simulation
734 suggested such transitions occur between the two domains of TcPOP exposing their catalytic site
735 during enzyme activity. Importantly, the β-propeller domain contributed to a high degree of movement
736 and instability, whereas, α/β hydrolase domain remained comparatively stable. Moreover, the Gibbs
737 free energy landscape of TcPOP indicated scattered blue spots, representing four-to-six major local
738 or global energy minima, and therefore, provided valuable insights into the presence of different
739 metastable states (Fig. 5a). Coincidentally, the number of minima matched the number of classes in
740 cryo-EM, possibly indicating that there might be a correlation between MD predictions and classes
741 distribution, which will be further investigated for methods development.

742 We, therefore, decided to analyse the structure using cryo-EM, despite the challenge to date of
743 resolving sub-80 kDa molecules, due to low image contrast[68]. To ensure the quality of samples before
744 data collection, we implemented a quality control pipeline, which included SEC-SAXS in solution
745 studies followed by assessment of the best buffer conditions using mass photometry to screen for the
746 best conditions for monodispersion, therefore increasing the chances of success.

747 Our approach led to determination of the TcPOP structure to 3.6 Å and 3.8 Å, respectively, in closed
748 and open conformation. This is one of the smallest cases, and at the highest resolution reported, in
749 terms of resolving multiple enzyme conformations in a vitreous state by single-particle cryo-EM[69]. Two
750 conformations of TcPOP could be easily identified in 3D classification spanning from fully closed to
751 fully open with an overall motion of ~ 22° between the two domains. The evident stability of the α/β
752 hydrolase domain observed in both open and closed conformations, as well as in those from aligned
753 cryo-EM maps, suggest possible region which are exposed to the immune system when the enzyme
754 is secreted in the blood, and therefore likely to include potential epitopes.

755 To confirm that these experimentally observed conformations exist in solution, optical tweezer studies
756 were performed in the presence and absence of substrate-mimicking peptide. Recent advances in
757 plasmonic nano-tweezers allowed us to sample conformational fluctuations of single proteins in
758 solution [70]. Our data show that TcPOP clearly fluctuates between open and closed states
759 independently from the presence of the substrate, confirming that the observed open and closed
760 conformations occur in solution and are observed without the usage of any additive. However, the
761 addition of the substrate-mimicking peptide affects the frequency at which the enzyme opens and
762 closes.

763 By HDX-MS, we primarily observed that selected helices and loops of the α/β-hydrolase domain and
764 a single loop of β-propeller domain (at the interface with the α/β-hydrolase domain) switch between
765 the two conformations via cooperative unfolding/refolding events along the protein backbone, which
766 are interpretable as long-lived perturbations of their secondary structure. This has been previously
767 observed for other enzymes[64]. Such a kinetic regime allowed us to understand the structural elements
768 of TcPOP switching between the closed and open conformation at different rates, which likely leads
769 the protein to occupy a multitude of intermediate states between the fully closed and fully open
770 conformation.

771 The intrinsic conformational heterogeneity in solution can pose great challenges to the structure
772 determination by cryo-EM, as multiple conformations merge into a single conformation. This often
773 leads to preferential orientation, eventually producing lower-resolution 3D reconstruction, which
774 requires the collection of large number of micrographs especially for small molecules, often in the
775 order of thousands. To overcome this barrier, we have analysed each of the distinct conformers with

776 DynaMight. Here, we have successfully characterized the open and close conformation of the vaccine
777 candidate TcPOP through a synergistic combination of *in silico*, structural, and in solution techniques.
778 We propose expanding this methodology for regular investigations of small, secreted proteins of sub-
779 80kDa size, especially when recalcitrant to crystallography approaches and where alternating
780 conformations in solution, are suspected. The addition of tilted data collection can also be beneficial
781 to alleviate preferential orientation, therefore reveal more structural details.

782 We envisage the possibility to extend this approach to other targets, allowing prediction of the number
783 of 3D classes in vitreous states using cryo-EM data based on MD simulations. In addition, it will
784 promote understanding of conformational heterogeneity at the early stages of cryo-EM data
785 processing and therefore, potentially aid future software developments towards this goal. We provide
786 experimental evidence on the distinct open and closed conformation, which will be invaluable to
787 determine which regions of TcPOP (and potentially other members of prolyl oligopeptidase family)
788 should be targeted to block the enzyme in either conformation, therefore aiding the development of
789 novel and much needed anti-parasitic therapeutic agents.

790 Additionally, we characterised anti-TcPOP polyclonal response, which revealed striking neutralising
791 properties with subsequent rapid lysis of trypomastigote. In addition, we isolated one monoclonal
792 antibody, which is also neutralising, but via other means. This information highlights TcPOP as a
793 priority vaccine target to be exploited for both, diagnostic and therapeutic solutions. Both are urgently
794 needed to reduce the burden of Chagas disease. In the longer-term, our findings will allow a structure-
795 guided development of a Chagas vaccine prototype, which is desperately needed in the fight against
796 this major neglected disease.

797

798 **Contributions**

799 S.B. expressed and purified proteins, characterised them biophysically and *in silico* and determined
800 the cryo-EM structure. S.B. and C.L. prepared the samples for cryo-EM data acquisition. S.B., T.J.R.,
801 and E.H. processed and analysed cryo-EM data. S.B. and A.M.F. isolated and purified antibodies.
802 L.B. immunised mice and performed FACS analysis. S.B., M.K. and W.B.S performed mass
803 photometry experiments and data analysis. V.C. designed, performed and analysed HDX-MS. M.A.
804 and C.Y. performed plasmonic optical tweezers studies. F.O. and J.M.K. performed infection and
805 parasite binding experiments. I.C. conceptualise the experiments and provided funding. S.B. F.O. and
806 I.C. prepared the manuscript and all authors contributed and commented on it.

807

Acknowledgements

We would like to acknowledge: Dr Nathan Cowieson and Dr Katsuaki Inoue for assisting data collection at B21 beamline (Diamond Light Source), Dr David Staunton (University of Oxford) for data collection of SEC-MALS, Dr Lei Xu (NTU) and Prof. Rahmani Mohsen (NTU) for advice on data analysis of plasmonic optical tweezers experiments. Additionally, we would like to thank, Anu Itansanmi-Ogundayomi (Federal University of Technology Akure, Nigeria), Dr Jody Winter (NTU) and Dr Richard Cowan (University of Leicester). We would like to acknowledge Dr Maria Bassi and Kasper H Björnsson (University of Copenhagen) for advising in antibody methodologies, Dr David Owens (electron Bio-Imaging Centre, Oxon, UK) to provide advice in cryo-EM data quality assessment during the review process and Richard Atherton (LSHTM) for assistance with parasite cultures.

The project was funded by: Wellcome grant 204801/Z/16/Z (IC), Royal Society grant IES\R2\232167 (IC). SB is supported by the Nottingham Trent Doctoral School studentship and LB is funded by Novo Nordisk Foundation (NNF170C0026778). FO contribution was supported by Plan Propio of the University of Granada Research Stimulation grant (PP2023.PRI.I.14). We acknowledge The Midlands Regional CryoEM Facility at the Leicester Institute of Structural and Chemical Biology (LISCB), major funding from MRC (MC_PC_17136).

REFERENCES

1 Organization, W. H. Ending the neglect to attain the sustainable development goals: a road map for neglected tropical diseases 2021–2030. 177 p. (2020). https://doi.org:https://www.who.int/publications/i/item/9789240010352

2 Medone, P., Ceccarelli, S., Parham, P. E., Figuera, A. & Rabinovich, J. E. The impact of climate change on the geographical distribution of two vectors of Chagas disease: implications for the force of infection. *Philos Trans R Soc Lond B Biol Sci* **370** (2015). https://doi.org:10.1098/rstb.2013.0560

3 Lee, B. Y., Bacon, K. M., Bottazzi, M. E. & Hotez, P. J. Global economic burden of Chagas disease: a computational simulation model. *Lancet Infect Dis* **13**, 342-348 (2013). https://doi.org:10.1016/s1473-3099(13)70002-1 PMID - 23395248

4 Coura, J. R. The main sceneries of Chagas disease transmission. The vectors, blood and oral transmissions--a comprehensive review. *Mem Inst Oswaldo Cruz* **110**, 277-282 (2015). https://doi.org:10.1590/0074-0276140362

5 Bonney, K. M., Luthringer, D. J., Kim, S. A., Garg, N. J. & Engman, D. M. Pathology and Pathogenesis of Chagas Heart Disease. *Annu Rev Pathol* **14**, 421-447 (2019). https://doi.org:10.1146/annurev-pathol-020117-043711

6 Mazzeti, A. L., Capelari-Oliveira, P., Bahia, M. T. & Mosqueira, V. C. F. Review on Experimental Treatment Strategies Against Trypanosoma cruzi. *J Exp Pharmacol* **13**, 409-432 (2021). https://doi.org:10.2147/JEP.S267378

7 Castro, J. A., de Mecca, M. M. & Bartel, L. C. Toxic side effects of drugs used to treat Chagas' disease (American trypanosomiasis). *Hum Exp Toxicol* **25**, 471-479 (2006). https://doi.org:10.1191/0960327106het653oa

8 Joselin, D. V. *et al.* Multiple Discrete Typing Units of Trypanosoma cruzi Infect Sylvatic Triatoma dimidiata and Panstrongylus rufotuberculatus in Southeast Mexico. *Am J Trop Med Hyg* **105**, 1042-1049 (2021). https://doi.org:10.4269/ajtmh.20-1574

9 Lima, L. *et al.* Genetic diversity of Trypanosoma cruzi in bats, and multilocus phylogenetic and phylogeographical analyses supporting Tcbat as an independent DTU (discrete typing unit). *Acta Trop* **151**, 166-177 (2015). https://doi.org:10.1016/j.actatropica.2015.07.015

10 Breniere, S. F., Waleckx, E. & Barnabe, C. Over Six Thousand Trypanosoma cruzi Strains Classified into Discrete Typing Units (DTUs): Attempt at an Inventory. *PLoS Negl Trop Dis* **10**, e0004792 (2016). https://doi.org:10.1371/journal.pntd.0004792

11 Porras, A. I. *et al.* Target Product Profile (TPP) for Chagas Disease Point-of-Care Diagnosis and Assessment of Response to Treatment. *PLoS Negl Trop Dis* **9**, e0003697 (2015). https://doi.org:10.1371/journal.pntd.0003697

12 Bivona, A. E. *et al.* Trypanosoma cruzi 80 kDa prolyl oligopeptidase (Tc80) as a novel immunogen for Chagas disease vaccine. *Plos Neglect Trop D* **12**, e0006384 - 0006323 (2018). https://doi.org:10.1371/journal.pntd.0006384

13 Grellier, P. *et al.* Trypanosoma cruzi prolyl oligopeptidase Tc80 is involved in nonphagocytic mammalian cell invasion by trypomastigotes. *Journal of Biological Chemistry* **276**, 47078 - 47086 (2001). https://doi.org:10.1074/jbc.m106017200

14 Macaluso, G. *et al.* A Review on the Immunological Response against Trypanosoma cruzi. *Pathogens* **12** (2023). https://doi.org:10.3390/pathogens12020282

15 Flavia Nardy, A., Freire-de-Lima, C. G. & Morrot, A. Immune Evasion Strategies of Trypanosoma cruzi. *J Immunol Res* **2015**, 178947 (2015). https://doi.org:10.1155/2015/178947

16 Cardoso, M. S., Reis-Cunha, J. L. & Bartholomeu, D. C. Evasion of the Immune Response by Trypanosoma cruzi during Acute Infection. *Front Immunol* **6**, 659 (2015). https://doi.org:10.3389/fimmu.2015.00659

17 Lasse, C. *et al.* Prolyl Oligopeptidase From Leishmania infantum: Biochemical Characterization and Involvement in Macrophage Infection. *Front Microbiol* **11**, 1060 (2020). https://doi.org:10.3389/fmicb.2020.01060 PMID - 32547514

18 Bastos, I. M. *et al.* Prolyl oligopeptidase of Trypanosoma brucei hydrolyzes native collagen, peptide hormones and is active in the plasma of infected mice. *Microbes Infect* **12**, 457-466 (2010). https://doi.org:10.1016/j.micinf.2010.02.007

19 Fajtova, P. *et al.* Prolyl Oligopeptidase from the Blood Fluke Schistosoma mansoni: From Functional Analysis to Anti-schistosomal Inhibitors. *PLoS Negl Trop Dis* **9**, e0003827 (2015). https://doi.org:10.1371/journal.pntd.0003827

20 Kaushik, S. & Sowdhamini, R. Distribution, classification, domain architectures and evolution of prolyl oligopeptidases in prokaryotic lineages. *BMC Genomics* **15**, 985 (2014). https://doi.org:10.1186/1471-2164-15-985

21 Fulop, V., Bocskei, Z. & Polgar, L. Prolyl oligopeptidase: an unusual beta-propeller domain regulates proteolysis. *Cell* **94**, 161-170 (1998). https://doi.org:10.1016/s0092-8674(00)81416-6

22 Bastos, Izabela M. D. *et al.* Molecular, functional and structural properties of the prolyl oligopeptidase of Trypanosoma cruzi (POP Tc80), which is required for parasite entry into mammalian cells. *Biochem J* **388**, 29-38 (2005). https://doi.org:10.1042/bj20041049 PMID - 15581422

23 UniProt, C. UniProt: the Universal Protein Knowledgebase in 2023. *Nucleic Acids Res* **51**, D523-D531 (2023). https://doi.org:10.1093/nar/gkac1052

24 Sayers, E. W. *et al.* Database resources of the National Center for Biotechnology Information. *Nucleic Acids Res* **52**, D33-D43 (2024). https://doi.org:10.1093/nar/gkad1044

25 Letunic, I. & Bork, P. Interactive Tree Of Life (iTOL) v5: an online tool for phylogenetic tree display and annotation. *Nucleic Acids Res* **49**, W293-W296 (2021). https://doi.org:10.1093/nar/gkab301

26 Edgar, R. C. MUSCLE: a multiple sequence alignment method with reduced time and space complexity. *BMC Bioinformatics* **5**, 113 (2004). https://doi.org:10.1186/1471-2105-5-113

27 Waterhouse, A. *et al.* SWISS-MODEL: homology modelling of protein structures and complexes. *Nucleic Acids Res* **46**, W296-W303 (2018). https://doi.org:10.1093/nar/gky427

28 Baek, M. *et al.* Accurate prediction of protein structures and interactions using a three-track neural network. *Science* **373**, 871-876 (2021). https://doi.org:10.1126/science.abj8754

29 Ashkenazy, H. *et al.* ConSurf 2016: an improved methodology to estimate and visualize evolutionary conservation in macromolecules. *Nucleic Acids Res* **44**, W344-350 (2016). https://doi.org:10.1093/nar/gkw408

30 Laskowski, R. A. & Thornton, J. M. PDBsum extras: SARS-CoV-2 and AlphaFold models. *Protein Sci* **31**, 283-289 (2022). https://doi.org:10.1002/pro.4238

31 Davis, I. W., Murray, L. W., Richardson, J. S. & Richardson, D. C. MOLPROBITY: structure validation and all-atom contact analysis for nucleic acids and their complexes. *Nucleic Acids Res* **32**, W615-619 (2004). https://doi.org:10.1093/nar/gkh398

32 Schrödinger L, D. W. PyMOL. *Internet access* (2024).

33 Knudsen, A. S. *et al.* Enhancing neutralization of Plasmodium falciparum using a novel monoclonal antibody against the rhoptry-associated membrane antigen. *Sci Rep* **12**, 3040 (2022). https://doi.org:10.1038/s41598-022-06921-1

34 Hopkins, J. B. BioXTAS RAW 2: new developments for a free open-source program for small-angle scattering data reduction and analysis. *J Appl Crystallogr* **57**, 194-208 (2024). https://doi.org:10.1107/S1600576723011019

35 Franke, D. *et al.* ATSAS 2.8: a comprehensive data analysis suite for small-angle scattering from macromolecular solutions. *J Appl Crystallogr* **50**, 1212-1225 (2017). https://doi.org:10.1107/S1600576717007786

36 Grant, T. D. electron density determination directly from solution scattering data. *Nature Methods* **15**, 191-+ (2018). https://doi.org:10.1038/Nmeth.4581

37 Svergun, D. I. Determination of the Regularization Parameter in Indirect-Transform Methods Using Perceptual Criteria. *Journal of Applied Crystallography* **25**, 495-503 (1992). https://doi.org:Doi 10.1107/S0021889892001663

38 Soltermann, F. *et al.* Quantifying Protein-Protein Interactions by Molecular Counting with Mass Photometry. *Angew Chem Int Ed Engl* **59**, 10774-10779 (2020). https://doi.org:10.1002/anie.202001578

39 Pronk, S. *et al.* GROMACS 4.5: a high-throughput and highly parallel open source molecular simulation toolkit. *Bioinformatics* **29**, 845-854 (2013). https://doi.org:10.1093/bioinformatics/btt055

40 Dari Kimanius, K. J., Max E Wilkinson, Sofia Lövestam, Vaithish Velazhahan, Takanori Nakane, Sjors H.W. Scheres. Data-driven regularisation lowers the size barrier of cryo-EM structure determination. *bioRXiv* (2023).
41 Rohou, A. & Grigorieff, N. CTFFIND4: Fast and accurate defocus estimation from electron micrographs. *J Struct Biol* **192**, 216-221 (2015). https://doi.org:10.1016/j.jsb.2015.08.008
42 Bepler, T. *et al.* Positive-unlabeled convolutional neural networks for particle picking in cryo-electron micrographs. *Nat Methods* **16**, 1153-1160 (2019). https://doi.org:10.1038/s41592-019-0575-8
43 Kimanius, D. *et al.* Data-driven regularization lowers the size barrier of cryo-EM structure determination. *Nat Methods* **21**, 1216-1221 (2024). https://doi.org:10.1038/s41592-024-02304-8
44 Schwab, J., Kimanius, D., Burt, A., Dendooven, T. & Scheres, S. H. W. DynaMight: estimating molecular motions with improved reconstruction from cryo-EM images. *Nat Methods* **21**, 1855-1862 (2024). https://doi.org:10.1038/s41592-024-02377-5
45 Sanchez-Garcia, R. *et al.* DeepEMhancer: a deep learning solution for cryo-EM volume post-processing. *Commun Biol* **4**, 874 (2021). https://doi.org:10.1038/s42003-021-02399-1
46 Millan, C., McCoy, A. J., Terwilliger, T. C. & Read, R. J. Likelihood-based docking of models into cryo-EM maps. *Acta Crystallogr D Struct Biol* **79**, 281-289 (2023). https://doi.org:10.1107/S2059798323001602
47 Emsley, P. & Cowtan, K. Coot: model-building tools for molecular graphics. *Acta Crystallogr D Biol Crystallogr* **60**, 2126-2132 (2004). https://doi.org:10.1107/S0907444904019158
48 Pettersen, E. F. *et al.* UCSF chimera - A visualization system for exploratory research and analysis. *Journal of Computational Chemistry* **25**, 1605-1612 (2004). https://doi.org:10.1002/jcc.20084
49 Tang, G. *et al.* EMAN2: An extensible image processing suite for electron microscopy. *Journal of Structural Biology* **157**, 38-46 (2007). https://doi.org:10.1016/j.jsb.2006.05.009
50 Pang, Y. & Gordon, R. Optical trapping of a single protein. *Nano Lett* **12**, 402-406 (2012). https://doi.org:10.1021/nl203719v
51 Yousefi, A. *et al.* Optical Monitoring of In Situ Iron Loading into Single, Native Ferritin Proteins. *Nano Lett* **23**, 3251-3258 (2023). https://doi.org:10.1021/acs.nanolett.3c00042
52 Xu, H., Jones, S., Choi, B. C. & Gordon, R. Characterization of Individual Magnetic Nanoparticles in Solution by Double Nanohole Optical Tweezers. *Nano Lett* **16**, 2639-2643 (2016). https://doi.org:10.1021/acs.nanolett.6b00288
53 Guttman, M., Weis, D. D., Engen, J. R. & Lee, K. K. Analysis of overlapped and noisy hydrogen/deuterium exchange mass spectra. *J Am Soc Mass Spectrom* **24**, 1906-1912 (2013). https://doi.org:10.1007/s13361-013-0727-5
54 Trelle, M. B., Madsen, J. B., Andreasen, P. A. & Jorgensen, T. J. Local transient unfolding of native state PAI-1 associated with serpin metastability. *Angew Chem Int Ed Engl* **53**, 9751-9754 (2014). https://doi.org:10.1002/anie.201402796
55 Merkle, P. S. *et al.* Substrate-modulated unwinding of transmembrane helices in the NSS transporter LeuT. *Sci Adv* **4**, eaar6179 (2018). https://doi.org:10.1126/sciadv.aar6179
56 Shan, L., Mathews, II & Khosla, C. Structural and mechanistic analysis of two prolyl endopeptidases: role of interdomain dynamics in catalysis and specificity. *Proc Natl Acad Sci U S A* **102**, 3599-3604 (2005). https://doi.org:10.1073/pnas.0408286102
57 Beltran-Hortelano, I. *et al.* Design and synthesis of Mannich base-type derivatives containing imidazole and benzimidazole as lead compounds for drug discovery in Chagas Disease. *Eur J Med Chem* **223**, 113646 (2021). https://doi.org:10.1016/j.ejmech.2021.113646

58 Tan, Y. Z. *et al.* Addressing preferred specimen orientation in single-particle cryo-EM through tilting. *Nature Methods* **14**, 793-+ (2017). https://doi.org:10.1038/Nmeth.4347

59 Liebschner, D. *et al.* Macromolecular structure determination using X-rays, neutrons and electrons: recent developments in Phenix. *Acta Crystallogr D Struct Biol* **75**, 861-877 (2019). https://doi.org:10.1107/S2059798319011471

60 Bastos, I. M. D. *et al.* Molecular, functional and structural properties of the prolyl oligopeptidase of
(POP Tc80), which is required for parasite entry into mammalian cells. *Biochem J* **388**, 29-38 (2005). https://doi.org:10.1042/Bj20041049

61 Hajizadeh, N. R., Franke, D., Jeffries, C. M. & Svergun, D. I. Consensus Bayesian assessment of protein molecular mass from solution X-ray scattering data. *Sci Rep* **8**, 7204 (2018). https://doi.org:10.1038/s41598-018-25355-2

62 Mohammad, T. *et al.* Impact of amino acid substitution in the kinase domain of Bruton tyrosine kinase and its association with X-linked agammaglobulinemia. *Int J Biol Macromol* **164**, 2399-2408 (2020). https://doi.org:10.1016/j.ijbiomac.2020.08.057

63 Hodge, E. A., Benhaim, M. A. & Lee, K. K. Bridging protein structure, dynamics, and function using hydrogen/deuterium-exchange mass spectrometry. *Protein Sci* **29**, 843-855 (2020). https://doi.org:10.1002/pro.3790

64 Trelle, M. B., Madsen, J. B., Andreasen, P. A. & Jorgensen, T. J. D. Local Transient Unfolding of Native State PAI-1 Associated with Serpin Metastability. *Angewandte Chemie-International Edition* **53**, 9751-9754 (2014). https://doi.org:10.1002/anie.201402796

65 Weis, D. D., Engen, J. R. & Kass, I. J. Semi-automated data processing of hydrogen exchange mass spectra using. *Journal of the American Society for Mass Spectrometry* **17**, 1700-1703 (2006). https://doi.org:10.1016/j.jasms.2006.07.025

66 Correia, B. E. *et al.* Proof of principle for epitope-focused vaccine design. *Nature* **507**, 201-206 (2014). https://doi.org:10.1038/nature12966

67 Walter, T. S. *et al.* Lysine methylation as a routine rescue strategy for protein crystallization. *Structure* **14**, 1617-1622 (2006). https://doi.org:10.1016/j.str.2006.09.005

68 Herzik, M. A., Jr., Wu, M. & Lander, G. C. High-resolution structure determination of sub-100 kDa complexes using conventional cryo-EM. *Nat Commun* **10**, 1032 (2019). https://doi.org:10.1038/s41467-019-08991-8

69 Lyumkis, D. Challenges and opportunities in cryo-EM single-particle analysis. *J Biol Chem* **294**, 5181-5197 (2019). https://doi.org:10.1074/jbc.REV118.005602

70 Awasthi, S., Ying, C., Li, J. & Mayer, M. Simultaneous Determination of the Size and Shape of Single alpha-Synuclein Oligomers in Solution. *ACS Nano* **17**, 12325-12335 (2023). https://doi.org:10.1021/acsnano.3c01393

i

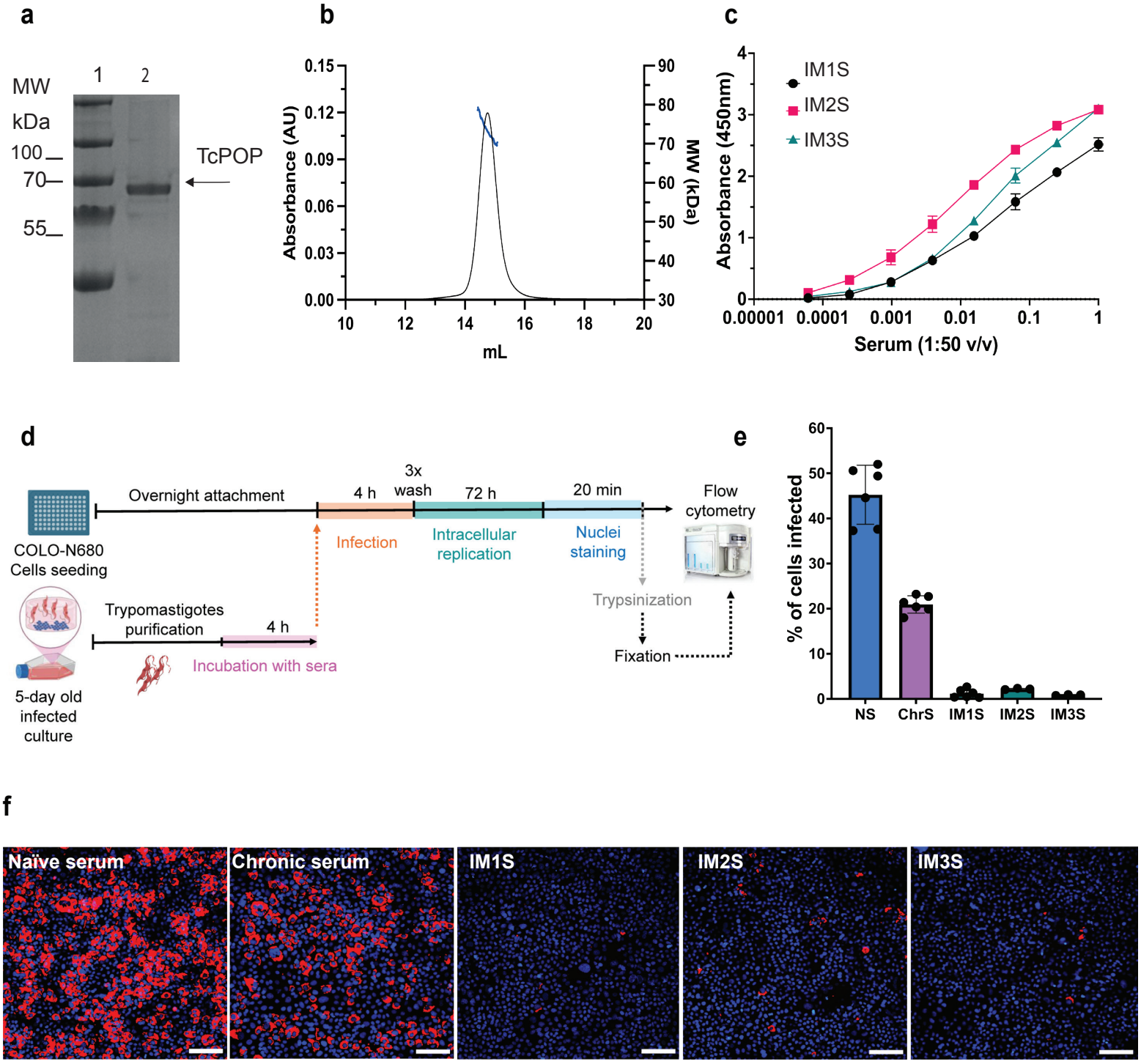
a
MW
kDa
1
2
100
70
55
TcPOP
b
Absorbance (AU)
MW (kDa)
mL
c
IM1S
IM2S
IM3S
Absorbance (450nm)
Serum (1:50 v/v)
d
Overnight attachment
4 h
3x wash
72 h
20 min
Flow cytometry
COLO-N680 Cells seeding
Infection
Intracellular replication
Nuclei staining
Trypsinization
Fixation
Trypomastigotes purification
4 h
Incubation with sera
5-day old infected culture
e
% of cells infected
NS
ChrS
IM1S
IM2S
IM3S
f
Naïve serum
Chronic serum
IM1S
IM2S
IM3S

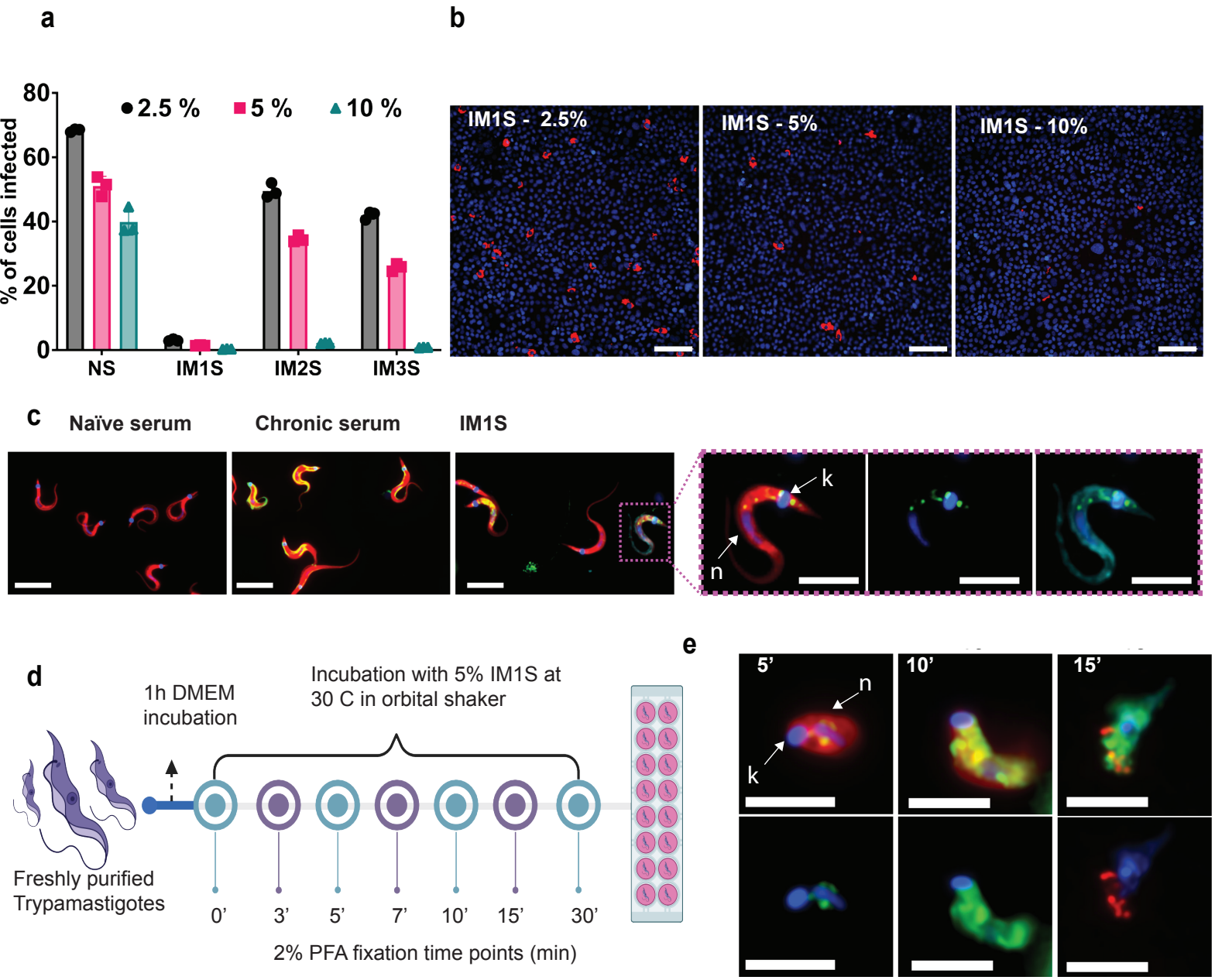
a
b
% of cells infected
80
60
40
20
0
2.5 %
5 %
10 %
NS
IM1S
IM2S
IM3S
IM1S - 2.5%
IM1S - 5%
IM1S - 10%
c
Naïve serum
Chronic serum
IM1S
k
n
d
1h DMEM incubation
Incubation with 5% IM1S at 30 C in orbital shaker
Freshly purified Trypamastigotes
0'
3'
5'
7'
10'
15'
30'
2% PFA fixation time points (min)
e
5'
10'
15'
n
k

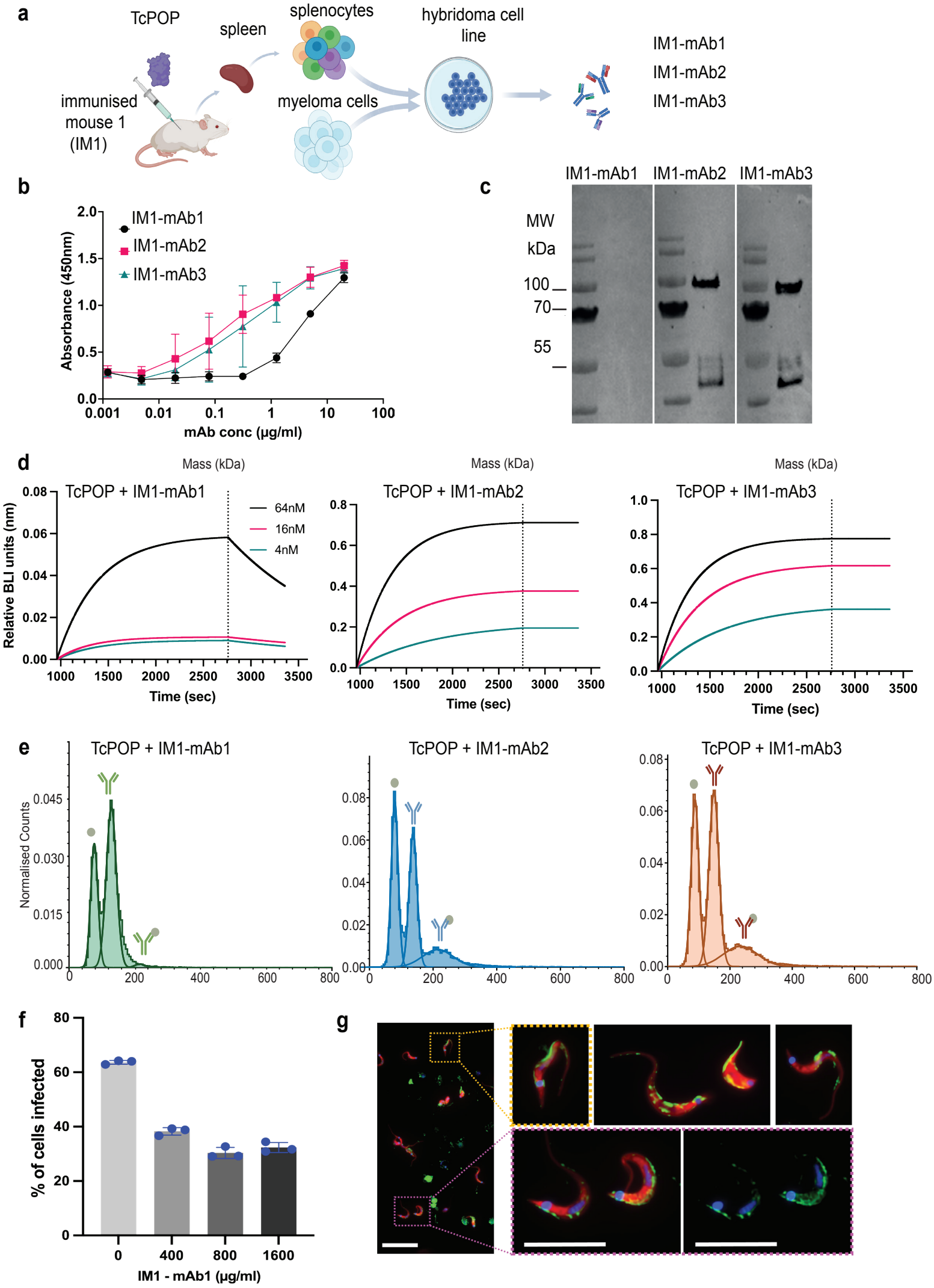
a
TcPOP
spleen
splenocytes
hybridoma cell line
immunised mouse 1 (IM1)
myeloma cells
IM1-mAb1
IM1-mAb2
IM1-mAb3
b
IM1-mAb1
IM1-mAb2
IM1-mAb3
Absorbance (450nm)
mAb conc (µg/ml)
c
IM1-mAb1
IM1-mAb2
IM1-mAb3
MW
kDa
100
70
55
d
Mass (kDa)
TcPOP + IM1-mAb1
TcPOP + IM1-mAb2
TcPOP + IM1-mAb3
64nM
16nM
4nM
Relative BLI units (nm)
Time (sec)
e
TcPOP + IM1-mAb1
TcPOP + IM1-mAb2
TcPOP + IM1-mAb3
Normalised Counts
f
% of cells infected
IM1 - mAb1 (µg/ml)
g

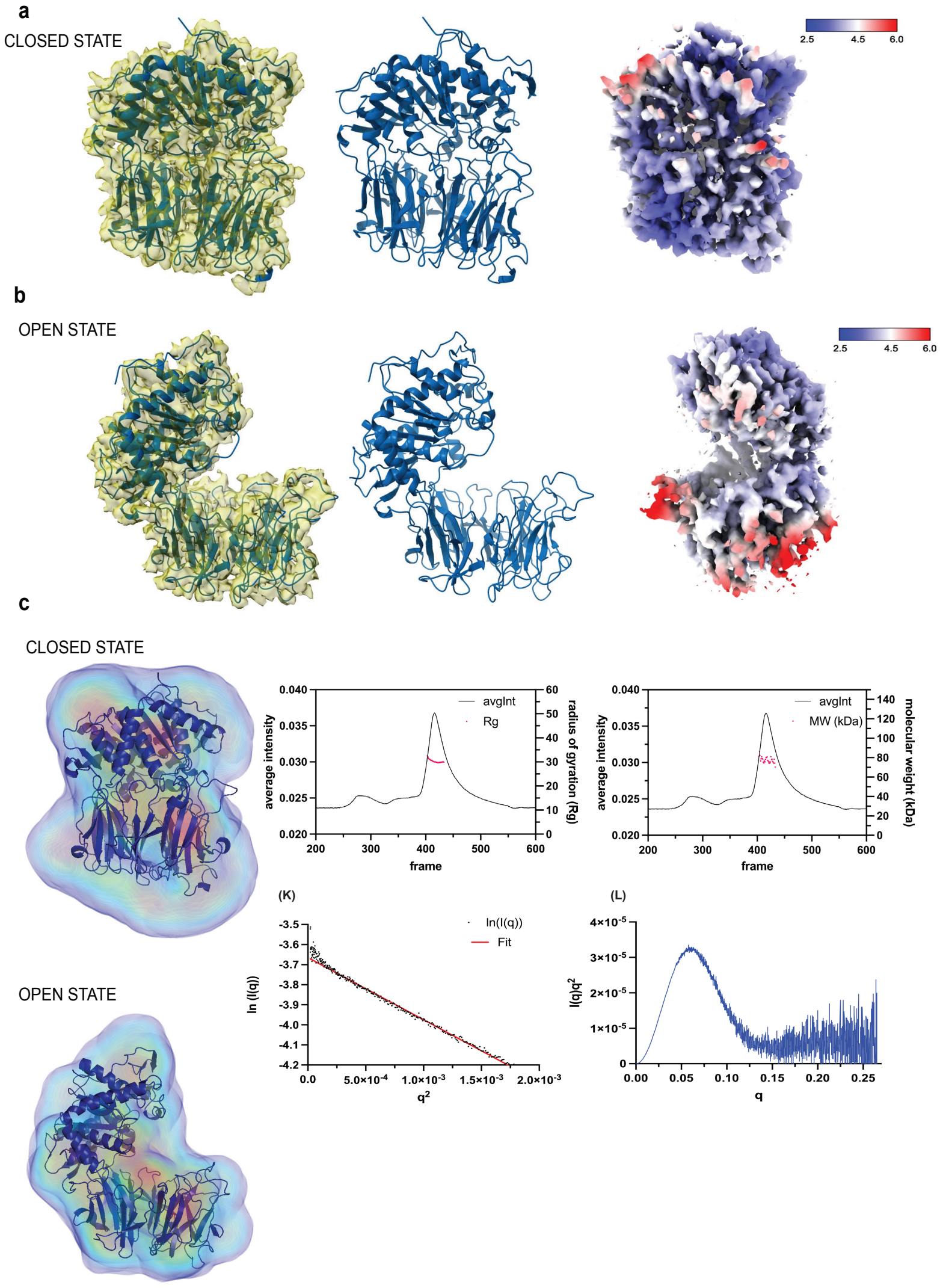
a
CLOSED STATE
2.5
4.5
6.0
b
OPEN STATE
2.5
4.5
6.0
c
CLOSED STATE
OPEN STATE
avgInt
Rg
average intensity
radius of gyration (Rg)
frame
avgInt
MW (kDa)
average intensity
molecular weight (kDa)
frame
(K)
ln(I(q))
Fit
ln (I(q))
q2
(L)
I(q)q2
q

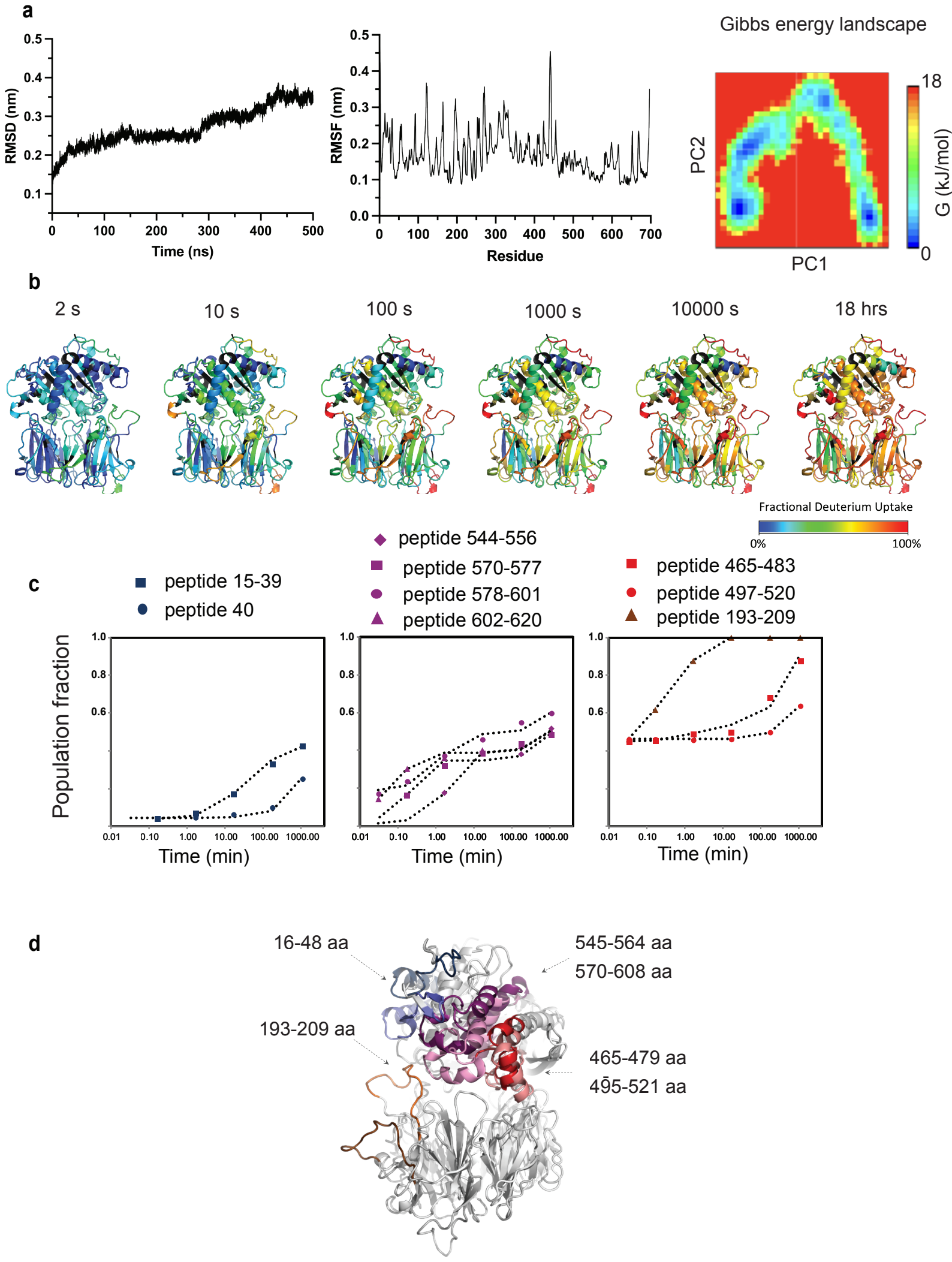
a
RMSD (nm)
Time (ns)
RMSF (nm)
Residue
Gibbs energy landscape
PC2
PC1
G (kJ/mol)
18
0
b
2 s
10 s
100 s
1000 s
10000 s
18 hrs
Fractional Deuterium Uptake
0%
100%
c
peptide 15-39
peptide 40
peptide 544-556
peptide 570-577
peptide 578-601
peptide 602-620
peptide 465-483
peptide 497-520
peptide 193-209
Population fraction
Time (min)
d
16-48 aa
545-564 aa
570-608 aa
193-209 aa
465-479 aa
495-521 aa